


Article

Genesis of the Bailugou Vein-Type Zinc-Lead-Silver Deposit, Eastern Qinling Orogen, China: Constraints from Ore Geology and Fluid Inclusions

Yan Yang^{1,2,*}, Nana Guo³, Hui Chen^{1,2}, Donghao Wu⁴, Zhenshan Pang^{1,2} and Yanjing Chen^{5,*} ¹ Development and Research Center, China Geological Survey, Beijing 100037, China² Technical Guidance Center for Mineral Exploration, Ministry of Natural Resources of the People's Republic of China, Beijing 100037, China³ Bureau of Natural Resources of Luanchuan County, Luoyang 471500, China⁴ School of Earth Sciences and Resources, China University of Geosciences, Beijing 100083, China⁵ Key Laboratory of Orogen and Crust Evolution, Peking University, Beijing 100871, China

* Correspondence: yyan@mail.cgs.gov.cn (Y.Y.); gigyjchen@126.com (Y.C.)

Abstract: The Bailugou vein-type zinc-lead-silver deposit is located in the Eastern Qinling Orogen, China. There has been a long-standing debate about whether its formation is related to magmatism or metamorphism. To determine the origin of ore-forming materials and fluids, we conducted a geological and fluid inclusion investigation of the Bailugou. Field surveys show that the vein-type orebodies are controlled by faults in the dolomitic marbles of the Mesoproterozoic Guandaokou Group, and they are distal to the regional Yanshanian intrusions. Four ore stages, i.e., quartz–pyrite ± sphalerite (Stage 1), quartz–polymetallic sulfides (Stage 2), dolomite–polymetallic sulfides (Stage 3), and calcite (Stage 4), are identified through microscopic observation. The homogenization temperatures of measured fluid inclusions vary in the range of 100 °C to 400 °C, with the dominating concentration at 350 °C to 400 °C, displaying a descending trend from early to late stages. The estimated formation depth of the Bailugou deposit varies from 2 km to 12 km, which is deeper than the metallogenic limit of the epithermal hydrothermal deposit but conforms to the typical characteristics of a fault-controlled deposit. The ore-forming fluid in Stage 1 originates from a fluid mixture and experiences a phase separation (or fluid immiscibility) between the metamorphic-sourced fluid and the fluids associated with ore-bearing carbonate-shale-chert association (CSC) strata. This process results in the transition to metamorphic hydrothermal fluid due to water–rock interactions in Stage 2, culminating in gradual weakening and potential fluid boiling during the mineralization of Stage 3. Collectively, the Bailugou lead-zinc-silver mineralization resembles an orogenic-type deposit formed by metamorphic fluids in the Qinling Yanshanian intracontinental orogeny.

Keywords: metamorphic hydrothermal; orogenic zinc-lead-silver ore deposit; Bailugou; fluid inclusions; Eastern Qinling Orogen



Citation: Yang, Y.; Guo, N.; Chen, H.; Wu, D.; Pang, Z.; Chen, Y. Genesis of the Bailugou Vein-Type Zinc-Lead-Silver Deposit, Eastern Qinling Orogen, China: Constraints from Ore Geology and Fluid Inclusions.

Minerals **2024**, *14*, 1119. <https://doi.org/10.3390/min14111119>

Academic Editor: Giorgio Garuti

Received: 29 July 2024

Revised: 17 September 2024

Accepted: 24 October 2024

Published: 4 November 2024



Copyright: © 2024 by the authors. Licensee MDPI, Basel, Switzerland. This article is an open access article distributed under the terms and conditions of the Creative Commons Attribution (CC BY) license (<https://creativecommons.org/licenses/by/4.0/>).

1. Introduction

Since the general classification scheme of silver-lead veins, according to dominant mineral assemblage, have been first proposed by Beck and Weed [1], the subdivisions and ore deposits within it have been frequently reorganized, renamed, or even changed according to new geologic observations or theories, especially for those vein-type Zn–Pb–Ag deposits genetically related to the intrusions, which are further described as the Cordilleran-type or skarn vein deposits, were well documented [2–9]. The veins, which are not genetically related to felsic intrusions but more commonly occur near a crustal-scale fault, are considered late features in the tectonic evolution of an orogen by Beaudoin and Sangster [10], based on a worldwide review of silver, lead, and zinc vein deposits from six districts: the Kokanee Range and Keno Hill (Canada), Coeur d’Alène (United States),

the Harz Mountains and Freiberg (Germany), and Příbram (Czechoslovak). Since then, more similar cases have been presented as orogenic or metamorphic hydrothermal Ag–Pb–Zn deposits [11–14]. Some of these vein-type deposits specially develop in Eastern Qinling Orogen, China, such as Tieluping [15], Lengshuibei [16], Yindonggou [17], Weishancheng [18,19], Shagou [20,21], Xiaguan [22], Longmendian [23], etc. Known as rich in the endowment of Mo–W–Fe–Ag–Pb–Zn (Figure 1), where the Nannihu Mo–W and Shangfanggou Mo–Fe super large deposits [24,25] were endowed, the Luanchuan area also developed several large to super-large vein-type zinc–lead (–silver) deposits, such as Lengshuibei, Bailugou, Yindonggou, Tudimiaogou, Banchang, discovered by the geological survey department of Henan Province in the 2000s [26]. The Lengshuibei, Bailugou, and Yindonggou zinc–lead–silver deposits were approximated with total predicted reserves of 20 Mt (Pb + Zn) and 19,000 t Ag [27]. There are still many critical issues in the genesis that are poorly understood and need to be thoroughly explored and specifically discussed. For example, what are the specific geological characteristics of vein-type zinc–lead (–Ag) deposits? What are the sources of ore-forming fluid and constituents? What is their detailed evolutionary process and genetic model? These are some of the questions that require further exploration and clarification.

Fluids are the primary carriers of mass and heat within the Earth's crust [28–30]. The flow of fluid, which can be of magmatic, metamorphic, connate, marine, or meteoric origin [31–33], leads to leaching, mobilization, and transport, finally depositing the elements of economic interest, which presents as hydrothermal ore deposits. The circulation of surface-derived fluids within the crust is enhanced by active crustal faults [34]. Thus, constraining the source of ore-forming fluids is critical to clarifying the origin of metallic elements during mineralization.

The Bailugou vein-type deposit in the Luanchuan area, Eastern Qinling Orogen, China, is located in the Lushi-Luanchuan WNW-trending fold-thrust belt, which is part of the Huaxiong terrane in the Eastern Qinling Orogen, southern margin of the North China Craton (Figure 1). The history of the discovery of the Bailugou lead-zinc deposit in Henan Province, China, goes back to the 1950s. Geologists first identified the presence of lead and zinc deposits in the area during geological prospecting activities. The mine was officially discovered and started to be further developed from the late 1950s onwards. Duan et al. studied the fluid inclusions of the Bailugou deposit briefly without dividing metallogenetic stages [35]. Although several studies about regionally developed deposits have been published [36–41], the genesis of the Bailugou vein-type zinc-lead-silver deposit remains ambiguous; moreover, the detailed evolutionary mechanism of ore-forming fluid in the Bailugou deposit still remains unclear and needs to be solved and explored. This study conducted detailed regional, field geological and petrographic observations, alteration characteristics, and microthermometric data of fluid inclusions of ore minerals and wall rock from the Bailugou Zn–Pb (–Ag) ore deposit. The present study proposes an investigation into the origin, evolution, and precipitation mechanism of ore-forming fluids at the Bailugou deposit. The primary objective is to thoroughly comprehend the nature and genesis of the Bailugou and analogous vein-type deposits in the Luanchuan area. The conclusions of this examination are anticipated to offer valuable insights for deposit exploration in the surrounding region.

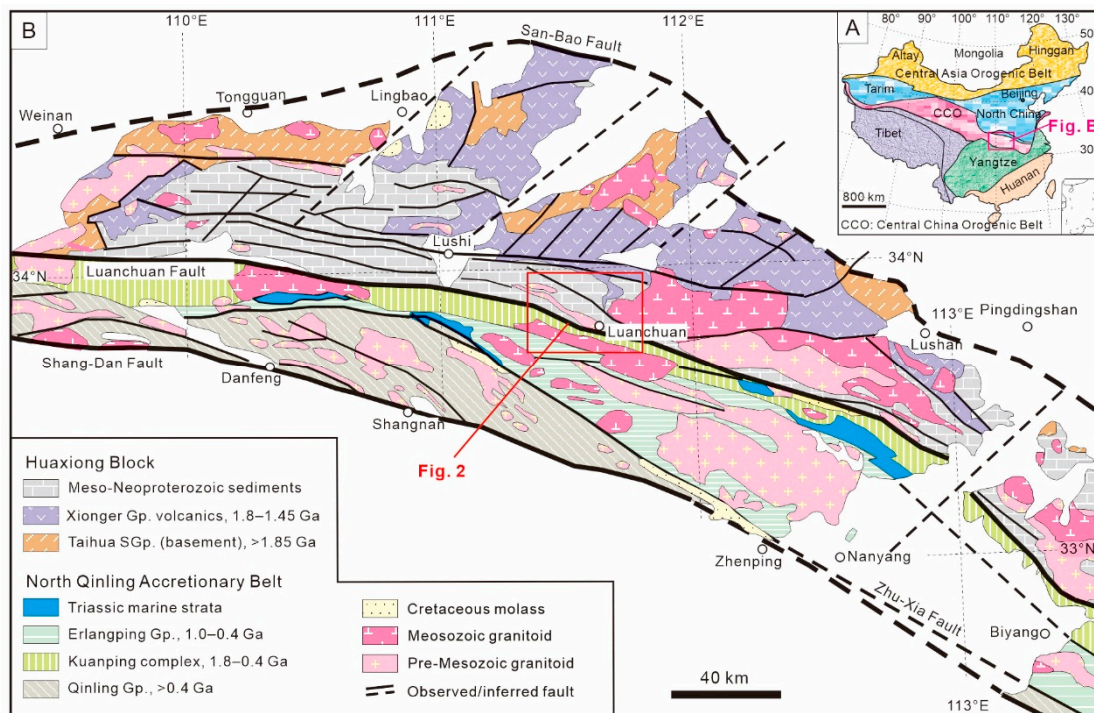


Figure 1. Geological map of the East Qinling area (modified from Li et al. [42]). (A) Tectonic map of China, showing the location of the Qinling Orogen; (B) tectonic subdivision of the Qinling Orogen, showing the location of the Bailugou Zn–Pb deposit.

2. Geological Setting

The tectonic evolution and regional metamorphism of the studied area shows that the Luanchuan Group and Guandaokou Group were sedimented under the forearc basin setting [43]. The primary lithology is mainly siliceous belt-bearing dolomite marble and medium-thick layered dolomite marble, containing conglomerate lithic sandstone, mudstone, sericite phyllite, calcareous phyllite, and metamorphic quartz dolomite, which is a CSC protolith formation that underwent greenschist facies metamorphism. The northwest fault structures in the area form the basic tectonic framework, characterized by large widths, long extensions, and dense distribution, controlling the distribution of strata in the region. A small number of tensional faults develop in the northeast direction. The intersections of these faults with the northwest-trending faults are the locations where ore bodies are hosted.

2.1. Stratigraphy

Strata in the Luanchuan area from base to top are as follows: (1) the Archean basement, Taihua Group, composed of amphibolite metamorphic complexes; (2) the Mesoproterozoic strata, the lower Xiong'er Group, consisting of andesitic-dacitic volcanic rocks, the upper Guandaokou Group, consisting of terrigenous clastic rocks and sedimentary carbonate formations; and (3) the Neoproterozoic strata of the lower Luanchuan Group, consisting of terrigenous clastic rocks, carbonate formations, and alkaline lavas, and the upper Taowan Group, composed of conglomerate and argillaceous carbonate rocks.

The Guandaokou and Luanchuan Groups extensively develop in the Bailugou Zn–Pb ore field (Figure 2) and are the primary ore-hosting strata of Mo–W–Fe and Zn–Pb–Ag ore deposits in this region. The Bailugou deposit was hosted in the dolomitic marble of the Mesoproterozoic Longjiayuan, Xunjiansi, Duguan, and Fengjiawan Formation of Guandaokou Group and the Neoproterozoic Baizhugou, Sanchuan and Nannihu Formation of Luanchuan Group (Figure 2).

The orebodies in the eastern and northern parts of the Bailugou Zn–Pb ore district are hosted in the Longjiayuan Formation (Figure 2). Meanwhile, the orebodies in the middle of the ore district are hosted in the Xunjiansi Formation, which conforms with the Longjiayuan Formation in the north and is fault-contacted with the Fengjiawan or Duguan Formation [44,45].

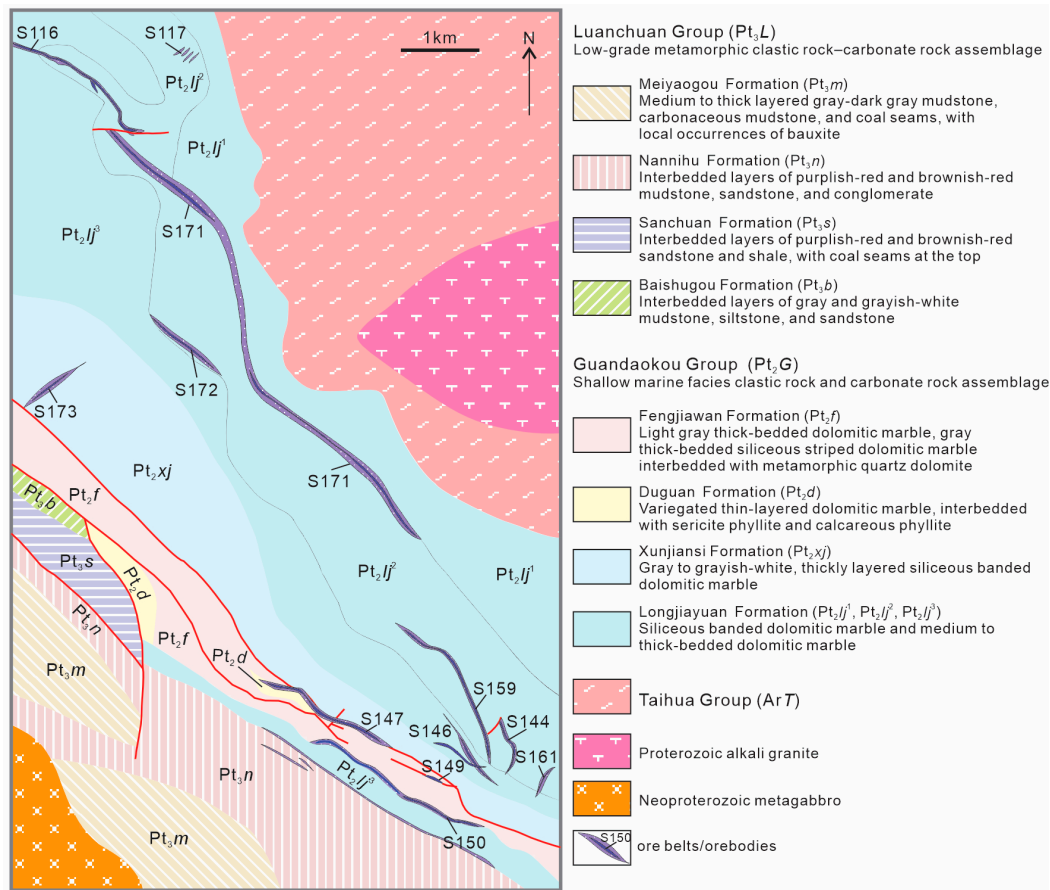


Figure 2. Geologic scheme of Bailugou Zn–Pb deposit (modified from Yan [45], Zhang [40]).

2.2. Igneous Rocks

There are two major phases of magmatic intrusion in the region. The earliest intrusion is the metagabbro in the Neoproterozoic Jingningian period, and the latter is the Mesoproterozoic Longwangzhuang alkaline granite (Figure 2). The Yanshanian intrusion was poorly outcropping.

The Longwangzhuang intrusion, which is the nearest intrusion to the Bailugou Zn–Pb ore bodies, lies in the east of the ore district, located in the core of the NWW-trending quaquaversal Niuxinduo plunging anticline. Hu et al. [43] suggested that the Longwangzhuang intrusion is A-type granite, the same age as the Luanchuan Group and formed under an extensional setting by 1235 Ma of Rb–Sr isochron age. However, according to a surface age of 1621 ± 16 Ma of zircons in Longwangzhuang potassium granite, Lu et al. [46] regarded it as the alkaline magmatism of the late period of the North China Craton break in 1800 Ma to 1600 Ma.

2.3. Structures

The ore district is located at the west limb of the Niuxinduo plunging anticline. The NWW-trending faults are the main ore-bearing structures that are well developed in the Bailugou Zn–Pb ore district (Figures 2 and 3). These faults mainly consist of SW strikes, with dips ranging from 35° to 79° and widths of 20–40 m, reaching a maximum of over

100 m [45]. A series of NE-NNE-trending faults occurred in the ore district, with SE-strike dips of 48° to 75° . The ore bodies are commonly located at the junctions of the NWW-trending faults and the NE-NNE-trending faults [44].

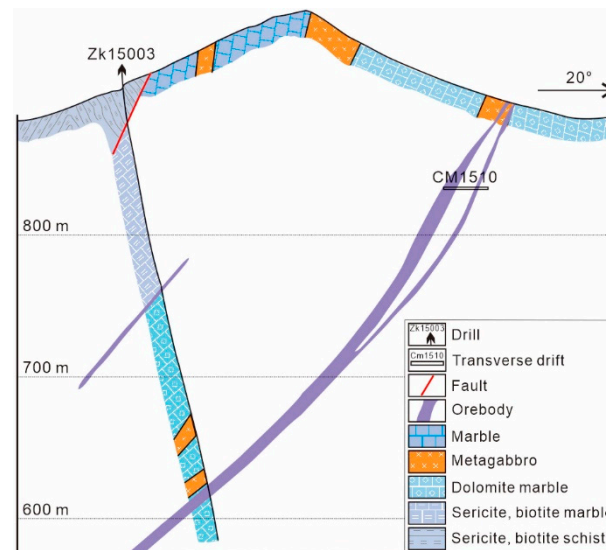


Figure 3. Geological sectional drawing of S150 mineralized zone of Bailugou deposit (modified from Yan et al. [47]).

3. Ore Geology

3.1. Ore Bodies

The Bailugou Pb-Zn-Ag deposit has a proved reserve of 198.92×10^4 t (Pb + Zn) and 2553.28 t Ag. The grade of the whole deposit is Pb@10.31%–16.43% with an avg. of 11.29%, Zn@2.33%–9.69% with an avg. of 5.58%, and Ag@ 80.18×10^{-6} – 279.18×10^{-6} with an avg. of 183.32×10^{-6} , respectively. The Bailugou ore deposit consists of four major mineralization zones: S150 in the south, S116 in the north, S171 and S172 in the central (Figure 2), and other small, low-grade mineralized zones. Strata and NE-trending faults control the occurrences of mineralized zones.

The S150 mineralized zone is located in the Luyuangou-Gongyingou area south of the ore district. The mineralized zone occurs in the fracture zone between the Longjiayuan Formation and Fengjiawan Formation of the Guandaokou Group (Figures 2 and 3). Silicified dolomite marble was developed in the fracture zone. The fracture zone is partially cataclastic rock and metagabbro veins. The S150 mineralized zone strikes 200° – 210° , dips at 50° – 70° , is distributed intermittently over 3000 m, spans widths of 2–6 m, with a maximum width of 20 m. Two bedded and stratoid ore bodies have been delineated; the ore bodies' occurrences are consistent with the strata. The ore grade has an increasing tendency from surface to deep [47].

The S116 mineralized zone is located in the northwest part of the Bailugou ore district, hosted in the talc-bearing quartz dolomite marble of the middle Longjiayuan Formation, Guandaokou Group. The S116 mineralized zone widths of 5–50 m extend over 3000 m, with an occurrence as a smooth-out wave shape with branches that leap along the strike (Figures 2 and 4). The fracture zones have dipped to NE with dips of 40° – 50° . The S116 mineralized zone mainly develops cataclastic rock while the compressed schistosity and mylonitization develop locally, and metagabbro veins fill occasionally. Four paralleled Zn–Pb–Ag ore bodies along the trending have been delineated. The No.1 main ore body has an occurrence as beds, stratoids, and veins, and their dips and strikes are consistent with the strata as synchronous folds. The ore body has a dip orientation of 40° and dip angles of 35° – 40° , while the length and depth are 1524 m and 50–60 m, respectively, and the thickness is 0.8–10.9 m with an average of 2.5 m.

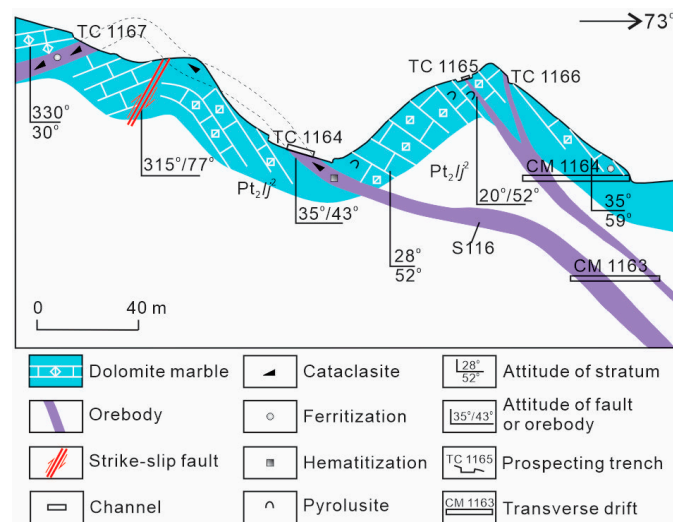


Figure 4. Geological sectional drawing of S116 mineralized zone of Bailugou deposit (modified from Yan [45]).

The S171 mineralized zone is geographically located through the Zhuyuangou, Bailugou, and Luyuangou area from west to east. The outcrop of S171 extended intermittently over 5000 m and a 2–6 m width with a maximum of 30 m. The ore bodies are located in the top part of the lower Longjiayuan Formation, distributed along NW-SE-trending as smooth-out waveforms (Figure 2). The S171 mineralized zone generally strikes NW, dips to SW with dip angles of 45° to 70°, and locally reverse dips along with the strata. The S171 mineralized zone dominantly developed taupe cataclastic silicified dolomite marble, ferritization–thematization cataclastic dolomite marble. The secondary was cataclastic with silicification, hematitization, ferritization, and iron-manganese. The wall rock was talc-bearing siliceous banding dolomite marble. There were 3 Zn–Pb–Ag ore bodies delineated at S171. The length of ore bodies was over 800 m, with stratoid and lens forms occurring—the strike of S171-1 and S171-2 ore bodies conform with the S171 mineralized zone.

The S172 mineralized zone is located on the top of the middle Longjiayuan Formation, paralleled with S171, dips to SW, with dip angles of 50°–70°. The ore bodies are longer than 300 m. The width of the ore bodies ranges from 1.0 to 2.5 m at the outcrop and 1.8–6.4 m at depth.

3.2. Mineral Assemblages

The ore minerals of S150 ore bodies include galena, sphalerite, pyrite, and minor amounts of chalcopyrite and argentite. The gangue minerals include quartz, dolomite, calcite, barite, sericite, talc, and are locally carbonaceous. The mineral grain size shows an increase with depth beneath the surface. The ore minerals of S116 ore bodies are mainly galena, followed by sphalerite, pyrite, and chalcopyrite. The gangue minerals include calcite, quartz, dolomite, and kaolinite. The S171 ore bodies developed pyritization in the deep, with ore minerals of galena, pyrite, and minor sphalerite. The gangue minerals include quartz, dolomite, calcite, talc, etc.

The ore structure is present as a disseminated, veinlet-disseminated, banded, massive, brecciated, veined, stockwork, and crystal cluster structure (Figure 5). The brecciated ores were striped or mottled early formed ores, cemented by hydrothermal ores and gangue minerals from later stages.

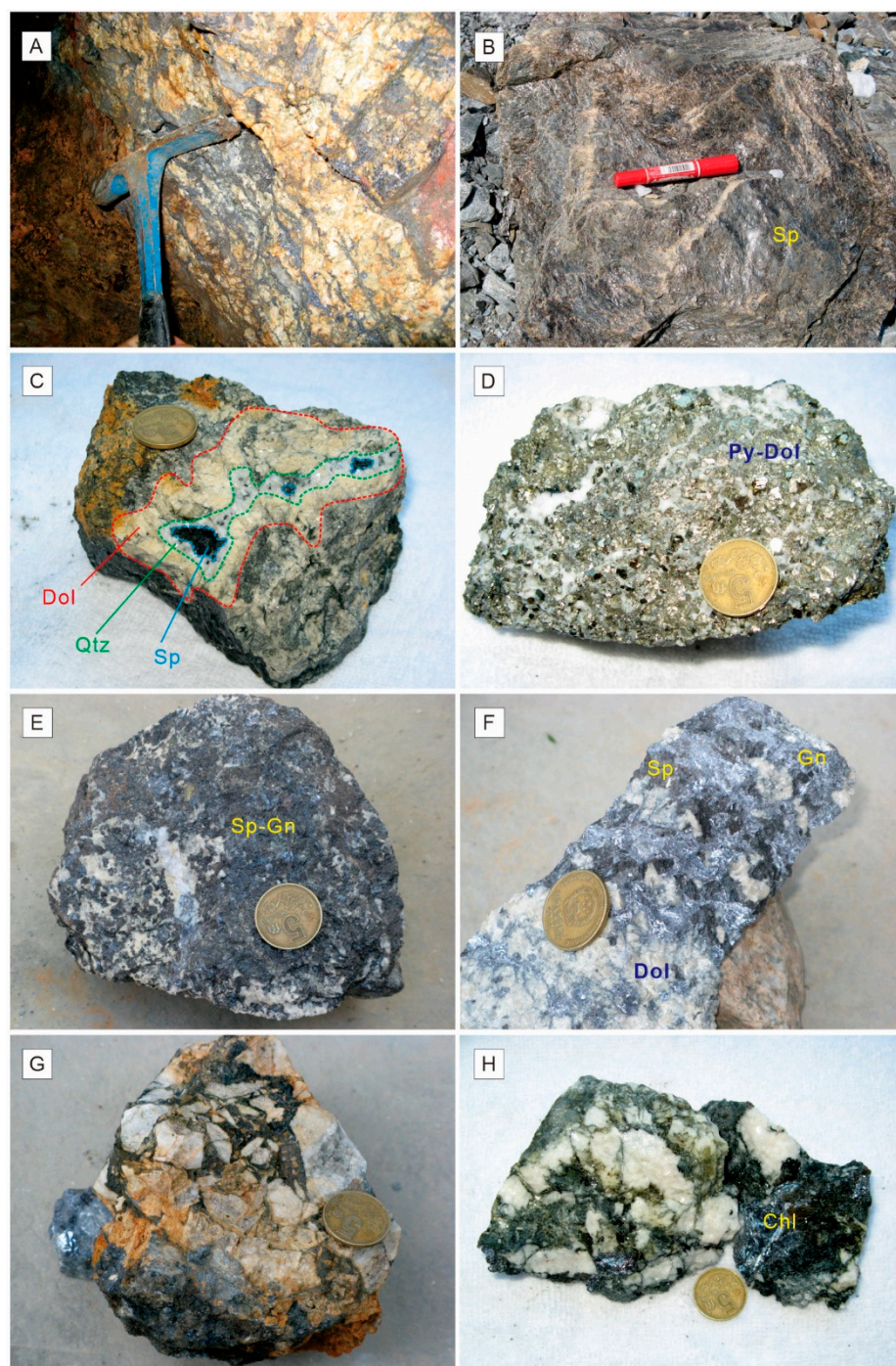


Figure 5. Ore structures of Bailugou deposit. (A) Ragged, banded distributes ores of galena (Gn), sphalerite (Sp) and dolomite (Dol); (B) massive ores of Sp; (C) Dol, quartz (Qtz) and Sp; (D) disseminated pyrite (Py) and Dol; (E) disseminated Sp, Gn and Dol; (F) banded Gn, Sp and Dol; (G) brecciated structures; (H) chloritization, chlorite (Chl).

The mineral texture is shown as granular texture, metasomatic dissolution, replacement, metasomatic etching texture, cataclastic structure, bird's-eye structure, residual skeleton texture (pyrite), growth girdle zone texture (sphalerite and dolomite) (Figures 5 and 6). Chalcopyrite is displayed as a beaded, emulsion droplet-like, or flake texture in the sphalerite as a solid solution separation structure only (Figure 6).

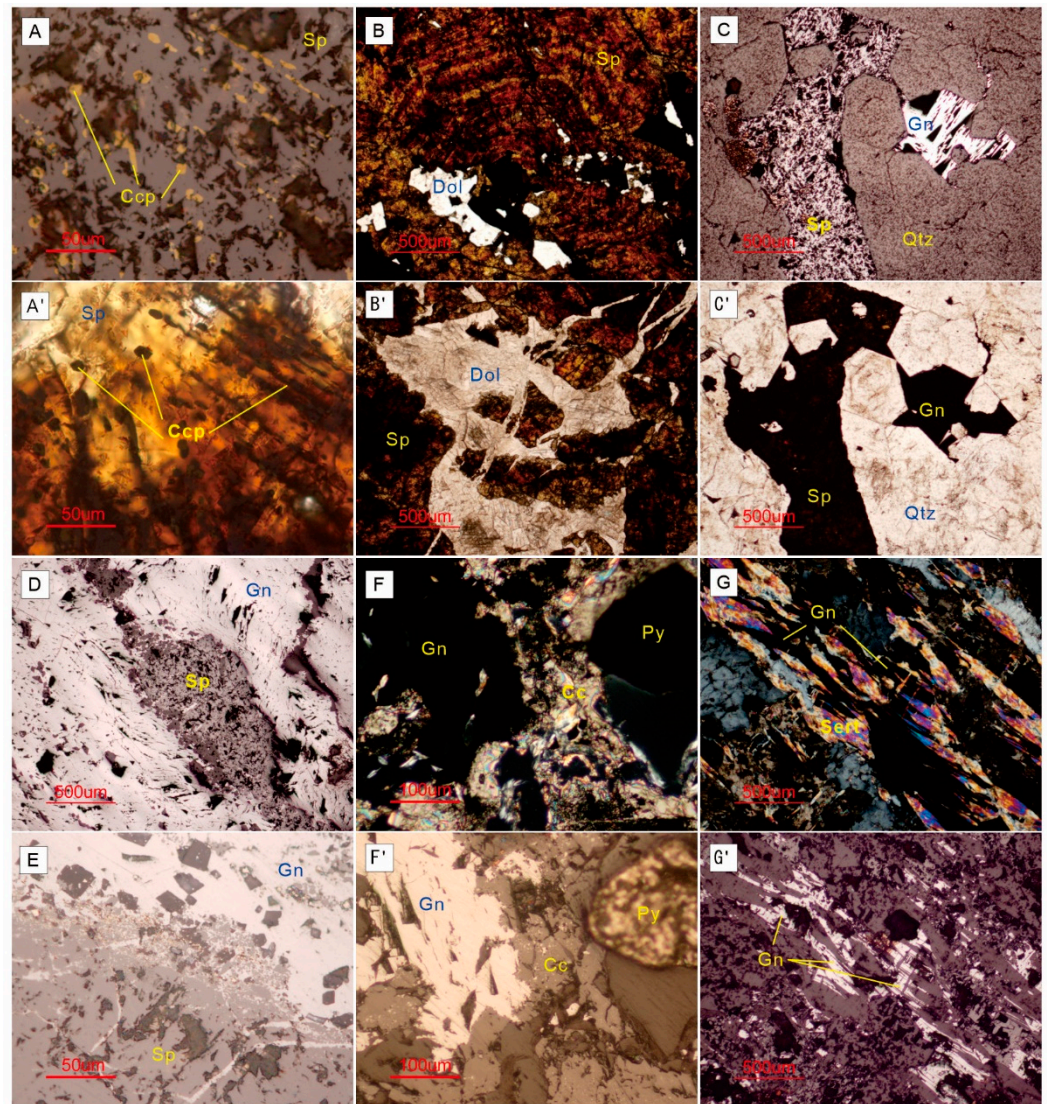


Figure 6. Ore textures of Bailugou deposit. (A) sphalerite (Sp)-chalcopyrite (Ccp) solid separation texture, chalcopyrite exhibit as bead-strings in sphalerite, under reflected light, (A') shows under the transmission light (-); (B) growth girdle zone of altered sphalerite backfilled by late dolomite (Dol), under transmission light (-), (B') shows fractured sphalerite backfilled by dolomite, under transmission light (-); (C) xenomorphic sphalerite and galena (Gn) backfilled in prior euhedral quartz (Qtz) granula, under reflected light, (C') shows under the transmission light (-); (D) later galena etching replace sphalerite, contact as wedge-shape, under reflected light; (E) galena etching replaced sphalerite, contact as wedge-shape, galena stellated in sphalerite, reflect light; (F) pyrite (Py) and galena with late calcite, under transmission light (+), (F') under reflected light; (G) ductile deformation of galena, Sericite (Sert) and quartz, shaping as lens, bird-eye, pressure-shadow, under transmission light (+), (G') under reflected light.

3.3. Alteration and Mineralized Stages

Hydrothermal alteration in the Bailugou deposit includes silicification, dolomitization, and carbonation. The dolomitization and silicification are closely related to Pb-Zn mineralization, while the carbonation usually develops later than the main mineralization. In addition, there is a small amount of altered mineral-talc, which only developed in the wall rocks of the ore body in S116 and S171 with high hematite and limonite.

Dolomitization is very common in this area and can be roughly divided into two categories: one is regional dolomitization, which is distributed in a large range far from the ores

and usually has no trace of ore mineralization; another is restricted to the mineralization range and has a close relationship with the ores.

The regional dolomitization developed in the mid-thick layer dolomite, quartz dolomite marble, or stromatolite-bearing dolomite marble; the dolomitic rocks are mainly formed in clumped, breccia-like irregular aggregate or along the sides of cracks. Dolomites of this category are idiomorphic and semi-idiomorphic crystals; the crystals are primarily arranged in a circular band with a diameter of 0.015 mm–4.45 mm and grayish-white, which can be clearly distinguished from marble by its coarser grain and lighter color. In consideration of the distribution of the regional dolomitization being related to the fault and not uniform, dolomite is developed as uneven clumps in marble, and its occurrence is inconsistent with the bedding occurrence; dolomitization can be manifested as epigenetic.

The ore-related dolomitization is distributed in a limited way with the polymetallic mineralization. Dolomites of this category are sparry white, transparent, and usually with fine irregular-shaped veins.

Based on structures and textures of ores and petrographic study, the mineralization process can be roughly ascertained from early to late as fine pyrite (Py)–quartz (Q), growth girdle zoned sphalerite (Sp), polymetallic sulfides (Ms), sphalerite-chalcopyrite solid separation + quartz + coarse euhedral pyrite + granulose dolomite (Dol)-galena, galena, magnetite vein, dolomite veinlets, and chlorination-calcite (Cc) (Figures 5 and 6).

Hydrothermal alteration and mineralization can be divided into four stages. Stage 1 is characterized by the assemblage of fine-grained pyrite + quartz ± sphalerite (Q–Py±Sp) (Figure 7). Pyrites are primarily fragmented and are usually replaced by sphalerite and galena. Stage 2 is marked by quartz-polymetallic sulfides (Q–Ms) (Figure 7). The metallic minerals in Stage 2 mainly include sphalerite with chalcopyrite solid solution, pyrite, and galena. Stage 3 is characterized by the widely distributed dolomite-polymetallic sulfides (Dol–Ms), dominated by galena, sphalerite, and minor pyrite (Figure 7). Stage 4 is mainly composed of carbonate with no sulfide (Cc), which crosscut the earlier veins and ores.

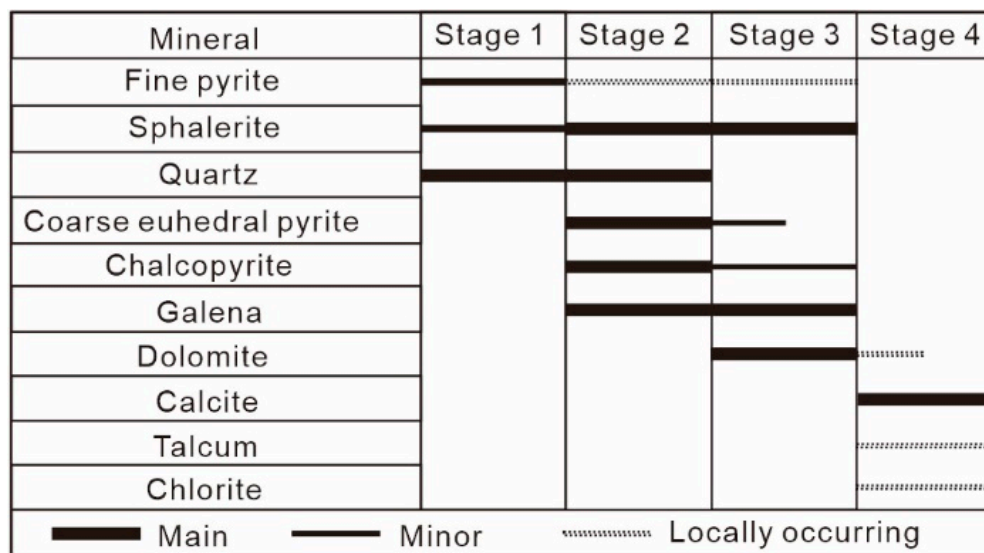


Figure 7. Paragenesis diagram of alteration assemblages showing sequence of mineralization at the Bailugou deposit.

4. Sampling and Analytical Methods for Fluid Inclusions

Samples used in this study were collected from the main orebodies of S150, S116, S171, and S147 in the Bailugou deposit (N 33°47'36"–N 33°48'36", E 111°38'32"–E 111°45'08"). Doubly polished sample thin sections, about 0.3 mm thick, were examined. Fluid inclusions in sphalerite, dolomite, and quartz were observed, respectively (Figure 8). Fluid inclusion observations were made using a standard optical petrographic microscope to identify

their genetic and composition types, vapor–liquid ratios, spatial clustering, and daughter minerals' species to document their paragenetic relationship. The volumetric fraction of phases in fluid inclusions was estimated at room temperature by reference to the volumetric chart of Roedder [48], using regular-shaped, flat inclusions whenever possible, according to the suggestion of Diamond [49]. These studies enabled successive assemblages of fluid inclusions to be defined. Representative samples of such assemblages were selected for detailed microthermometric and laser Raman spectroscopic studies.

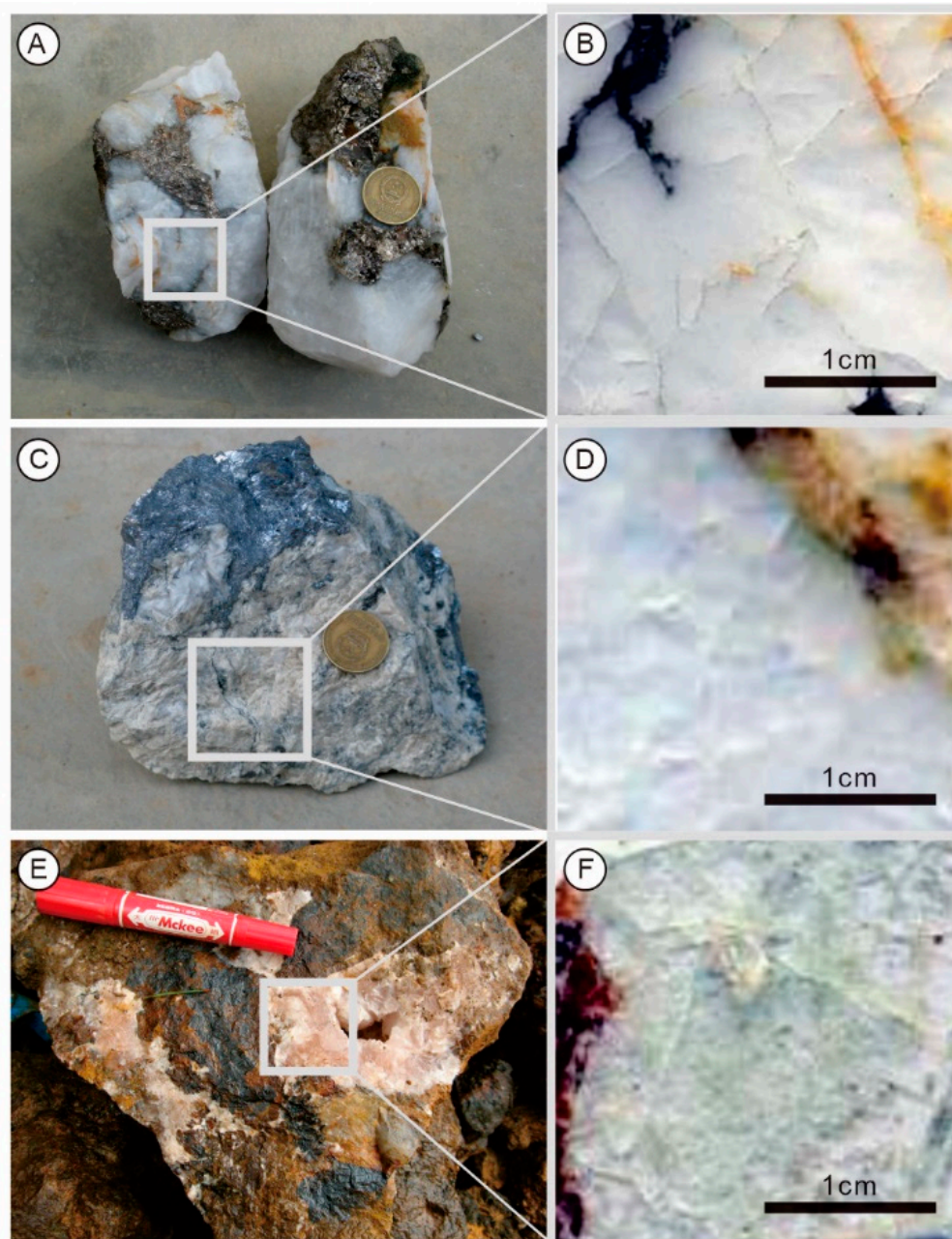


Figure 8. Petrography characteristics of FI samples at the Bailugou deposit. (A,B), quartz in stage 2 (Q–Ms); (C,D), dolomite in stage 3 (Dol–Ms); (E,F), calcite in stage 4 (Cc).

All fluid inclusion microthermometric measurements were performed on a Linkam THMSG600 heating-freezing stage mounted on a Leica microscope coupled to an image analysis system at the Fluid Inclusion Laboratory of the Key Laboratory of Mineralogy and Metallogeny, Guangzhou Institute of Geochemistry, Chinese Academy of Sciences.

The temperature range of the Linkam THMSG 600 heating-freezing stage was between 196° and 600 °C. Stage calibration was carried out at −56.6 °C, −10.7 °C, and 0 °C using synthetic FIs supplied by Fluid Inc. (Denver, CO). The uncertainty of the measurements is ± 0.5 °C for temperatures between −120° and −70 °C, ± 0.2 °C for the interval of −70° to +100 °C, and ± 2 °C for temperatures between 100° and 500 °C. All fluid inclusions were analyzed by freezing to −180 °C and heating up at a rate of 0.2 °C/min to 5 °C/min. The heating rate was reduced from 0.2 °C/min to 0.5 °C/min near the phase change points. Melting temperatures of solid CO₂ (T_{m,CO_2}), the freezing point of NaCl–H₂O inclusions ($T_{m,ice}$), final melting temperatures of clathrate ($T_{m,cla}$), homogenization temperatures of the CO₂ phase (T_{h,CO_2}), dissolution temperatures of daughter minerals ($T_{m,d}$) and total homogenization temperatures of FIs (T_h) were measured.

Compositions of individual fluid inclusions that are representative of specific stages, including vapor, liquid, and daughter mineral phases, were analyzed using RM-2000 Laser Raman spectroscopy at the Fluid Inclusion Laboratory of State Key Laboratory of Lithospheric Evolution, Institute of Geology and Geophysics, Chinese Academy of Sciences. An argon laser with a wavelength of 514.5 nm was used as the laser source at a power of 1000 mW. Integration time was 10 s to 30 s, with ten accumulations for each spectral line. The spectral resolution was ± 2 cm^{−1} with a beam size of 1 μm. The instrumental setting was kept constant during all analyses.

For volatile-rich fluid inclusions, CO₂ was identified by melting a solid phase in inclusions below −56.6 °C. Based on Burke [50], the molar fractions of CO₂, CH₄, and N₂ were determined.

Salinities of CO₂–H₂O, NaCl–H₂O, and halite-bearing FIs (expressed as wt%NaCl equiv.) were estimated by the clathrate melting temperatures of CO₂-clathrate [48,51], last ice melting temperatures [52–54] and halite dissolution temperatures [53,55], respectively. The density of CO₂ in C-type FIs was estimated using the Flicor program [56] and the Brown and Lamb formula [57] for the H₂O–CO₂–NaCl system. The bulk density of W-type and S-type FIs was estimated using the formula of Haas [58] and Bodnar et al. [59], the bulk density of C-type was estimated using the Flicor program [56], and the formula of Brown and Lamb [57] for the H₂O–CO₂–NaCl system.

The trapping pressure of W-type FIs was estimated using the formula of Haas [58] and the phase diagram of Bischoff [60]; the trapping pressure of C-type FIs was estimated using the Flicor program [58], and the formula of Bowers and Helgeson [61] for the H₂O–CO₂–NaCl system; trapping pressure of S-type FIs was estimated using the formula seen in Bischoff [60].

5. Results

5.1. Petrography and Types of Fluid Inclusions

Fluid inclusions (FIs) in sphalerite are tiny and small in quantity, making it challenging to observe. The overall distribution of FIs in dolomite and quartz was generally scattered and random, and there were occasional isolated distributions with no obvious directionality. Secondary FIs are clustered along trails, crosscutting grains, or grain boundaries. Most FIs were observed in calcite with about 40 μm in diameter and minor in quantity distributed sporadically. Primary FIs observed in this study mainly have negative crystal, elongated, or irregular shapes, sub-roundness, triangle, strip-type, fusiform, and square shapes. The diameters of primary inclusions of varying sizes are smaller than 2 μm, more extensive than 20 μm, and concentrated in a range of 5 μm to 12 μm.

Fluid inclusions were classified into three types based on their appearance at 25 °C and by their Raman spectra and occur in successive stages of the vein and alteration paragenesis (Figure 9).

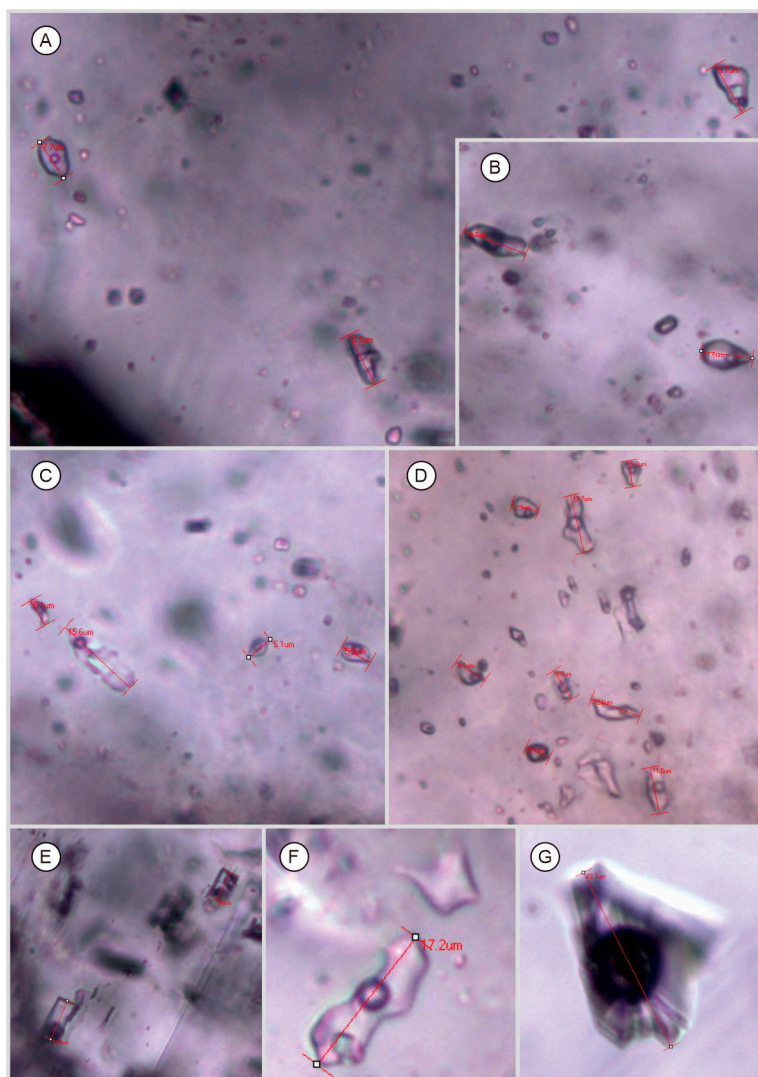


Figure 9. Microphotographs of fluid inclusions in samples from Bailugou deposit. All the pictures took under polarized light; (A) W-type and S-type FIs in quartz of sample BLC-30-2 (thin section) of stage 1 (Q-Py±Sp); (B) W-type and C-type FIs in quartz of sample BLC-30-12 (thin section) of stage 1; (C) S-type FIs in quartz of sample BGL-5-10 (thin section) of stage 1; (D) W-type FIs in quartz of sample BLC-33-2 (thin section) of stage 2 (Q-Ms); (E) W-type and C-S-type FIs in dolomite of sample BJD-2-11 (thin section) of stage 3 (Dol-Ms); (F) PL-type and S-type FI in dolomite of sample BP-8-2 (thin section) of stage 3; (G) W-type FI in calcite of sample B1471-3 (thin section) of stage 4 (Cc).

W-type: namely, NaCl–H₂O type FIs, which are two-phase (V_{H₂O}–L_{H₂O}) aqueous inclusions, can be further divided into three subtypes: (1) FIs, which are liquid-rich aqueous inclusions with 5 vol.% to 30 vol.% of a low-density vapor bubble at room temperature (Figure 9A–G); (2) Pure liquid (PL-type) FIs, which are gas-rich aqueous inclusions with gas filling degrees (ratio of V/(V + L)), most of which are smaller than 5%; and (3) Pure gas (PV-type) FIs, which are liquid-rich aqueous inclusions with gas filling degrees bigger than 80%.

S-type: namely, daughter minerals bearing FIs. Daughter minerals were detected mainly as light green cubic or roundness salt (Figure 9B–F), generally smaller than 20 vol.% S-type FIs were observed in the first three stages.

C-type: CO₂ bearing FIs, two- or three-phase aqueous-carbonic inclusions with a carbonic (vapor + CO₂ liquid) fraction of 20 vol.% to 40 vol.%. These FIs are mainly developed in the early and middle mineralized stage, about 10 vol.% to 20 vol.% of total

FIs. C-type FIs are generally of 10 μm to 15 μm in diameter and can be subdivided into two subtypes: (1) CO_2 -rich three-phase ($V_{\text{CO}_2} + L_{\text{CO}_2} + L_{\text{H}_2\text{O}}$) FIs at room temperature, which has CO_2 gas of 20 vol.% to 40 vol.% of the whole FI; (2) CO_2 -bearing two-phase FIs, which contain a gas phase of CO_2 and H_2O ($V_{\text{CO}_2+\text{H}_2\text{O}}$) and a liquid phase of H_2O ($L_{\text{H}_2\text{O}}$) (Figure 9B, E). The gas generally occupies 10 vol.% to 20 vol.% of the whole FI. Most C-type FIs in samples from the Bailugou deposit belong to this subtype.

5.2. Composition from Laser Raman Spectroscopy Detection

Laser Raman spectroscopy analyses of representative fluid inclusions have revealed that the main component of the inclusions' liquid phase is the H_2O (Figure 10A,C,D) ion occasionally. The volatile phase is of the inclusions mainly composed of CO_2 , H_2O , N_2 (with Raman peaks of 2327 cm^{-1} to 2329 cm^{-1} , Figure 10A–D), with minor CH_4 (with Raman peaks of 2913 cm^{-1} to 2919 cm^{-1} , Figure 10B) by chance. Daughter minerals detected in some FIs can be identified as thenardite (with Raman peaks of 1159 cm^{-1} , Figure 10B–D).

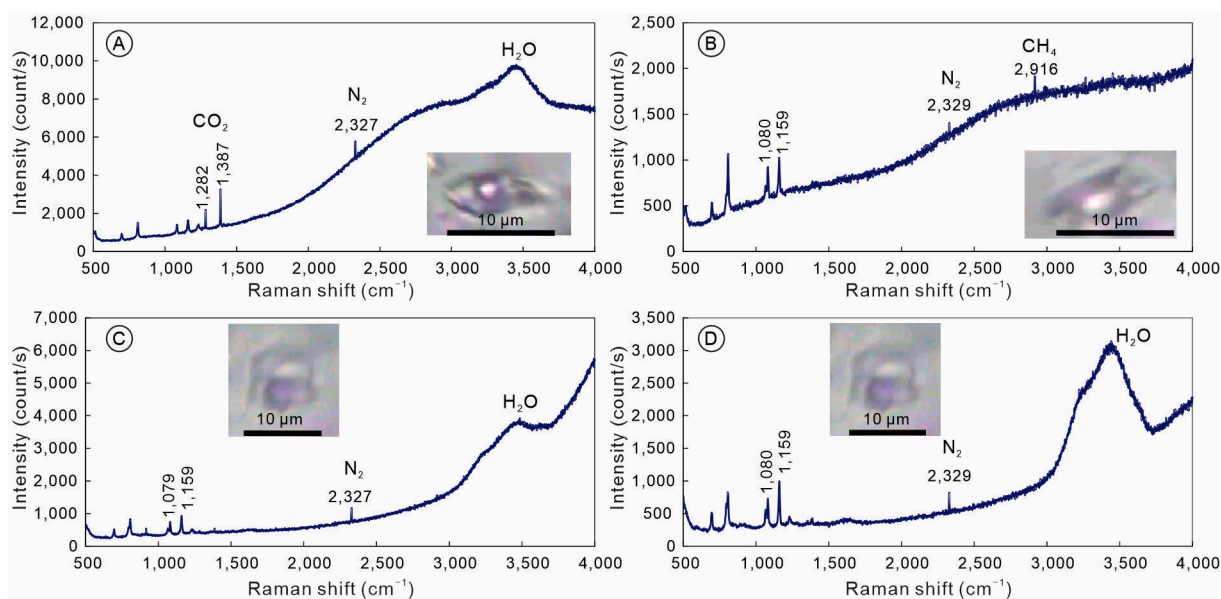


Figure 10. Representative Raman spectra of FIs from Bailugou deposit. (A) Raman spectrum of FI in sample BLC-30 of stage 1 (Q-Py±Sp), the compositions of volatile were mainly CO_2 , N_2 , and H_2O ; (B) Raman spectrum of the same inclusion as in Figure (A), mainly contain N_2 and CH_4 , also might contain daughter mineral of thenardite (1159 cm^{-1}); (C) Raman spectrum of FI in sample BLC-33 of stage 2 (Q-MS), the compositions of volatile were mainly CO_2 and N_2 , and possibly with daughter mineral of thenardite nearby the detected bubble (1159 cm^{-1}); (D) Raman spectrum of the same inclusion as in Figure (C), which mainly consists of H_2O , with minor CO_2 and N_2 , and possibly with daughter mineral of thenardite (1159 cm^{-1}).

5.3. Microthermometry

Microthermometric measurements were conducted on FIs in nine representative samples of different mineralization stages from the Bailugou deposit. Microthermometric data and relative parameters are summarized in Table 1 and Figure 11.

Table 1. Microthermometric data, salinity, density, pressure, and depth of the Bailugou deposit.

Stage	Sample no.	Host	Type	Size	Vapor	T_{mCO_2}	$T_{m_{cla}}$	Th_{CO_2}	T_{m_s}	Th_{tot} ²		$T_{m_{ice}}$	Salinity ³		Density of CO ₂	Bulk Density	Pressure	Lithostatic Depth	Hydrostatic Depth
		Minerals		(μ m)	(vol.%)	(°C)	(°C)	(°C) ¹	(°C)	(°C)	Counts	(°C)	(wt%NaCl eqv).	Counts	(g/cm ³) ⁴	(g/cm ³) ⁵	(MPa) ⁶	(km) ⁷	(km)
1	BGL-5	Qtz	W	4–10	5–30					115.6–345.3	29	−8.3 to −0.8	1.4–12.0	17	0.67–0.98	2–122	0.01–0.45	0.02–1.25	
	BGL-5	Qtz	C	5–19	30–80	−61.6 to −60.2	4.5–6.7	27.2–30.6		251.5–341.5	8		6.2–9.7	8	0.56–0.67	0.74–0.93	740–1157	2.70–4.22	7.55–11.81
	BGL-5	Qtz	S	4–16	5–10, 20–30				185.2–258.3	117.5–275.4	5		31.2–35.2	4	1.07–1.28	9–32	0.03–0.12	0.09–0.32	
	BLC-30	Qtz	W	5–15	5–30, 60					219.1–396.1	6	−13.8 to −4.8	7.6–17.6	3	0.76–0.92	21–183	0.08–0.67	0.22–1.86	
	BLC-30	Qtz	C	7–21	5, 95	−57.1 to −33.6	−21.3 to −19.5	−8 to −5.2		236.9–268.3	3								
	BLC-30	Qtz	S	4–13	5–30				101.2–320.8	213.5–482.7	12		28.0–39.8	12	0.89–1.15	1–76	0–0.28	0.01–0.77	
	BLC-13	Qtz	W	7–38	5–30					219.4–311.2	2	−9.7 to −6.7	10.1–13.6	3	0.84–1.08	0–91	0–0.33	0–0.93	
	BLC-13	Qtz	S	11–17	30–60				>560	252.4–407.2	3								
2	BLC-33	Qtz	W	4–13	5–30, 60					145.5–333.5	28	−15.5 to −4.0	6.4–19.0	12	0.83–0.98	4–119	0.01–0.44	0.44–1.22	
	BLC-33	Qtz	C	5–14	5–30		4.8–8.0	24.3–26.2		230.1–327.0	7		3.9–9.4	4	0.69	0.93	744	2.71	7.59
	BP-8	Qtz	W	4–18	5–30					208.7–247.5	32	−10.8 to −3.3	5.4–14.8	29	0.85–0.96	17–36	0.06–0.13	0.18–0.36	
	BP-8	Qtz	S	10–13	5–10				>400	180.2–239.7	2								
3	BGL-12	Dol	W	5–11	5–30, 60					228.5–301.2	7	−7.1 to −4.6	7.3–10.6	6	0.82–0.91	25–68	0.09–0.25	0.26–0.69	
	BJD-2	Dol	W	4–34	5–30, 60					106.2–281.2	18	−7.2 to −2.7	4.5–10.7	11	0.78–0.91	24–64	0.09–0.23	0.25–0.65	
	BP-8	Dol	W	4–51	5–30, 60					110.1–272.4	22	−8.0 to 0.0	0–11.7	21	0.77–0.97	1–54	0.01–0.20	0.01–0.56	
4	B1471	Cc	W	42–88	20–30					120.8–194.6	3								

Abbreviations: Qtz = Quartz; Cc = Calcite; Dol = Dolomite; T_{mCO_2} = melting temperature of solid CO₂; $T_{m_{ice}}$ = ice-melting temperature; $T_{m_{cla}}$ = clathrate dissociation temperature; Th_{CO_2} = homogenization temperature of CO₂; T_{m_s} = melting temperature of daughter mineral; Th_{tot} = total homogenization temperature; L and V stand for liquid and vapor to which the FIs homogenize, respectively. ¹ All the CO₂ phase of C-type FIs partial homogenize to liquid. ² Most FIs totally homogenize to liquid and few to vapor occasionally. ³ Salinity of W-type estimated by final ice melting temperature [52–54], salinity of C-type estimated by clathrate melting temperature [48,51], salinity of S-type estimated by halite dissolution temperatures [53,55]. ⁴ Density of CO₂ in C-type FIs estimated using the FIncor program [56] and the formula of Brown and Lamb [57] for the H₂O-CO₂-NaCl system. ⁵ Bulk density of W-type and S-type FIs estimated using the formula of Haas [58] and Bodnar et al. [59], bulk density of C-type estimated using the FIncor program [56], and the formula of Brown and Lamb [57] for the H₂O-CO₂-NaCl system. ⁶ Trapping pressure of C-type FIs estimated using the FIncor program [56] and the formula of Bowers and Helgeson [61] for the H₂O-CO₂-NaCl system. ⁷ The density of overlying rocks is supposed to be 2.8 g/cm³.

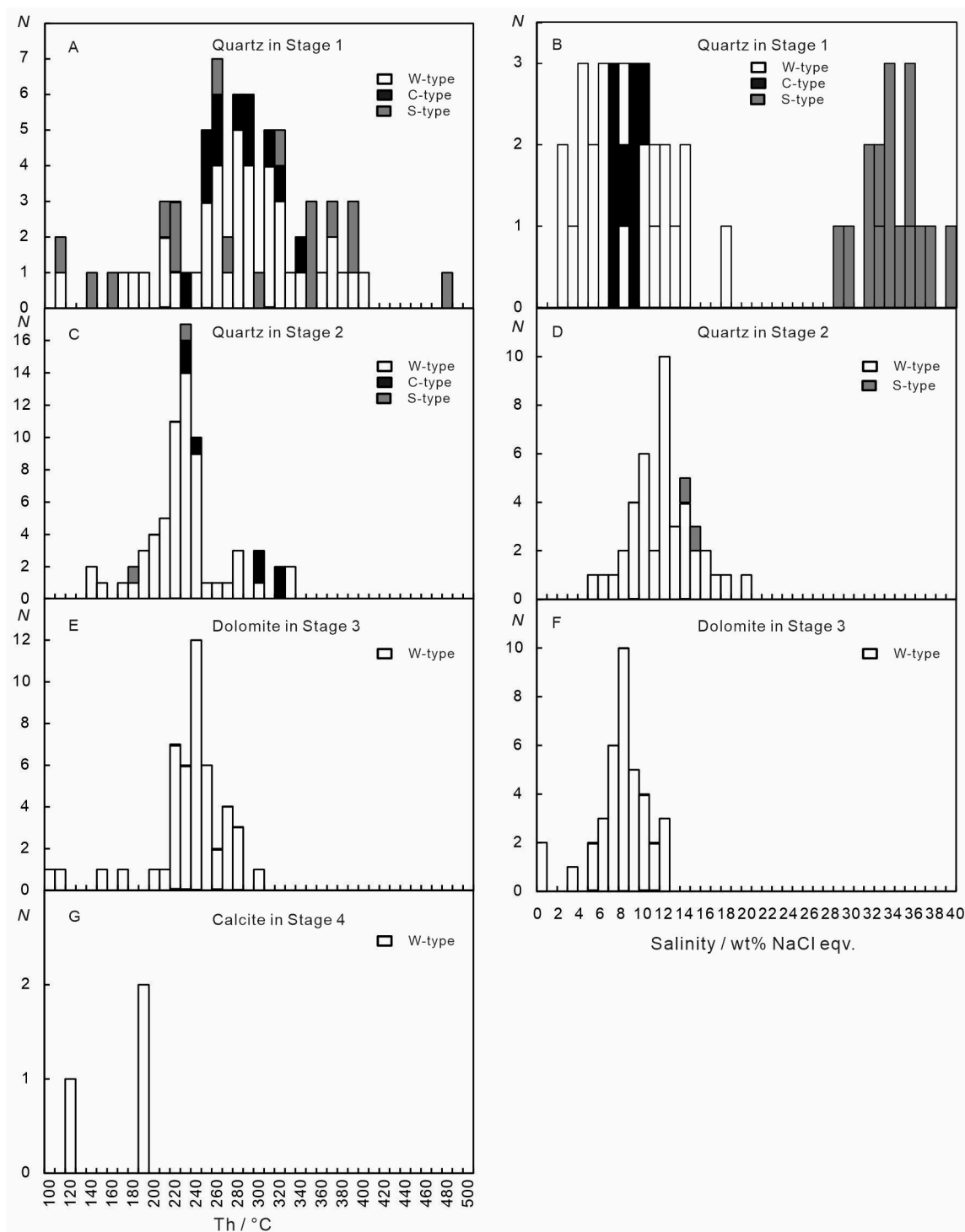


Figure 11. Histograms of homogenization temperatures and salinities of fluid inclusions of the Bailugou deposit.

In Stage 1, observation of FIs in quartz shows that mainly W-type FIs were detected with a size of 4 μm to 38 μm and a phase accounting for 5 vol.% to 30 vol.% normally. The W-type FIs' ice-melting temperatures are between $-13.8\text{ }^{\circ}\text{C}$ and $-0.8\text{ }^{\circ}\text{C}$ (Table 1), yielding salinities as 1.4 wt.% to 17.6 wt.% NaCl equiv. (Table 1, Figure 11), which are homogenized to liquid with the Th_{tot} values ranging from 115.6 $^{\circ}\text{C}$ to 396.1 $^{\circ}\text{C}$, clustered in the intervals of 250 $^{\circ}\text{C}$ to 350 $^{\circ}\text{C}$ and peaking at 300 $^{\circ}\text{C}$ (Figure 11). Their densities range from 0.56 g/cm^3 to 0.67 g/cm^3 . Beyond W-type FIs, there is a small amount of C-type FIs

and S-type FIs. The clathrate dissociation temperature of C-type FIs is 4.5 °C to 6.7 °C, with corresponding salinities of 6.2 wt.% to 9.7 wt.% NaCl equiv. (Table 1, Figure 11). The carbonic phase is partially homogenized to liquid at temperatures between 27.2 °C and 30.6 °C, while homogenized to liquid at temperatures ranging from 251.5 °C to 341.5 °C with bulk densities ranging from 0.74 g/cm³ to 0.93 g/cm³. The melting temperatures of daughter minerals observed in S-type FIs range from 101.2 °C to 320.8 °C, while the vapor phases are homogenized to liquid at 117.5 °C to 482.7 °C, corresponding to salinities of 28.0 wt.% to 39.8 wt.% NaCl equiv. (Table 1, Figure 11).

In Stage 2, the observation of FIs in quartz shows that main W-type FIs were detected with a size of 4 µm to 18 µm and phase accounting for 5 vol.% to 30 vol.% normally. The ice-melting temperatures of W-type FIs are between −15.5 °C and −3.3 °C (Table 1), yielding salinities of 5.4 wt.% to 19.0 wt.% NaCl equiv. (Table 1, Figure 11), which are homogenized to liquid with the $T_{h_{tot}}$ values ranging from 145.5 °C to 333.5 °C, visibly clustered in the intervals of 200 °C to 250 °C and peaking at 250 °C (Figure 11). Their densities range from 0.83 g/cm³ to 0.98 g/cm³. Besides W-type FIs, there is a small amount of C-type FIs and S-type FIs. The clathrate dissociation temperature of C-type FIs is 4.8 °C to 8.0 °C, with corresponding salinities of 3.9 wt.% to 9.4 wt.% NaCl equiv. (Table 1, Figure 11). The carbonic phase is partially homogenized to liquid at temperatures between 24.3 °C and 26.2 °C while homogenized to liquid at temperatures ranging from 230.1 °C to 327.0 °C with a bulk density of 0.93 g/cm³ (Table 1, Figure 11). Two S-type FIs in quartz in Stage 2 are observed. Still, the daughter minerals have higher melting temperatures than 550 °C, which has not been observed because it exceeded the heating limit of the Linkam THMSG600 heating-freezing units. In contrast, the vapor phase is homogenized to liquid at 180.2 °C and 239.7 °C (Table 1, Figure 11), close to the $T_{h_{tot}}$ of W-type and C-type. It is indicated that the trapping fluid is probably either a supersaturated solution, the daughter minerals were forecrystallized before being captured, or the inclusions were stretched in nature or during laboratory heating.

In Stage 3, W-type FIs are the main FI types detected with 4 µm–51 µm and a phase accounting for 5 vol.% to 30 vol.% normally. The W-type FIs' ice-melting temperatures are between −8.0 °C and 0 °C (Table 1), yielding salinities of 0 wt.% to 11.7 wt.% NaCl equiv. (Table 1, Figure 11), which are homogenized to liquid with $T_{h_{tot}}$ values ranging from 106.2 °C to 396.1 °C, clustered in the intervals of 200 °C to 300 °C and peaking at 250 °C (Figure 11). Their densities range from 0.77 g/cm³ to 0.97 g/cm³.

In Stage 4, only a tiny amount of W-type FIs are detected in calcite, which homogenized to liquid with the $T_{h_{tot}}$ values ranging from 120.8 °C to 194.6 °C (Table 1), clustered mainly in the intervals of 100 °C to 200 °C (Figure 11). W-type FIs are about 42 µm to 88 µm and phase accounting for 20 vol.% to 30 vol.% typically. The W-type FIs' ice-melting temperatures are failed observations because of the crystalline nature of host minerals. Still, the estimated salinity and density should be lower than Stage 1 to Stage 3, according to the behavior characteristics of those FIs during microthermometric measurements.

Based on the microthermometric measurements, the temperature range and its peak value at Stage 1, Stage 2, Stage 3, and Stage 4 of the Bailugou deposit show a decreasing trend from the early to late mineralization stage. The overall mineralization temperature range is about 400 °C to 100 °C (Table 1, Figure 11), belonging to a medium-temperature deposit.

6. Discussion

6.1. Fluid Salinity, Density, Pressure, and Ore-Forming Depth

6.1.1. Fluid Salinity and Density Estimated by FIs

The salinities of W-type FIs in Stage 1, Stage 2, and Stage 3 of the Bailugou deposit are estimated based on the microthermometric data, showing as 1.4 wt.% to 17.6 wt.% NaCl equiv, 5.4 wt.% to 19.0 wt.% NaCl equiv, 0 wt.% to 11.7 wt.% NaCl equiv, respectively (Table 1, Figure 11), which is relatively low and has an extensive variation range. The drift of salinity range indicates relatively low to high salinity levels during the initial mineralization

stage, which remains relatively high in the later stage, indicating the fluids continued to be concentrated and may have been influenced by hydrothermal processes, then showed a decline in salinity levels, even with some inclusions showing no salinity at all, which indicates a transition to lower salinity conditions. The salinities of C-type FIs in Stage 1 and Stage 2 are estimated as 6.2 wt.% to 9.7 wt.% NaCl equiv and 3.9 wt.% to 9.4 wt.% NaCl equiv, showing that the salinity reduced gradually from the early to late stages of mineralization. The salinity of S-type FIs in Stage 1 is estimated as 28.0 wt.% to 39.8 wt.% NaCl equiv, showing a character of medium-high salinity of initial ore-forming fluid.

The fluid density in Stage 1 is 0.67 g/cm³ to 0.98 g/cm³ for W-type, 0.74 g/cm³ to 0.93 g/cm³ for C-type, and 1.07 g/cm³ to 1.28 g/cm³ for S-type. The fluid density in Stage 2 is 0.83 g/cm³ to 0.98 g/cm³ for W-type and 0.93 g/cm³ for C-type. The fluid density in Stage 3 is 0.77 g/cm³ to 0.97 g/cm³ for W-type. Overall, the fluid density changes slightly through each stage. The Bailugou deposit remains a medium-high-density fluid during mineralization.

In summary, the medium-high density and salinity often suggests that the initial ore-forming fluid is derived from magmatic or metamorphic sources. Since the lack of outcroppings of intrusion in this area, the metamorphic source was more accepted. The coexistence of medium-high density and elevated temperatures meant more minerals could be dissolved and greater quantities of metals were transported, which are critical for the formation of economically viable mineral deposits. Furthermore, the density of the fluid can also provide insights into the pressure conditions during mineralization, and high density initial fluids in the Bailugou deposit are associated with great depths and pressures, suggesting that the mineralization occurred in a deep geological setting.

6.1.2. Ore-Forming Pressure and Depth

Trapping pressures and mineralization depths of Stage 1 are estimated according to Th_{tot} values of W-type FIs, Th_{CO_2} values, homogenization behaviors, and the proportion of the CO₂ phase in the C-type FIs and the melting temperatures of daughter minerals in S-type FIs, respectively (Table 1). The minimum trapping pressure for W-type FIs in Stage 1 is 0 MPa to 183 MPa, and the corresponding mineralization depths under lithostatic to supra-lithostatic pressures and hydrostatic pressures are 0 to 0.67 km and 0 to 1.86 km, respectively (Table 1). The minimum trapping pressures for C-type FIs in Stage 1 is 740 MPa to 1157 MPa, and the corresponding mineralization depths under lithostatic to supra-lithostatic pressures and hydrostatic pressures are 2.70 km to 4.22 km and 7.55 km to 11.81 km, respectively (Table 1). The minimum trapping pressures for S-type FIs in Stage 1 are 1 MPa to 76 MPa, and the corresponding ore-forming depths under lithostatic to supra lithostatic pressures and hydrostatic pressures are 0 to 0.28 km and 0 to 0.93 km, respectively (Table 1).

The estimated minimum trapping pressures for W-type FIs in Stage 2 are 4 MPa to 119 MPa, and the corresponding mineralization depths under lithostatic to supra lithostatic pressures and hydrostatic pressures are 0.01 km to 0.44 km and 0.18 km to 1.22 km, respectively (Table 1). The minimum trapping pressures for C-type FIs in Stage 2 is 744 MPa, and the corresponding ore-forming depths under lithostatic to supra lithostatic pressures and hydrostatic pressures are 2.71 km and 7.59 km, respectively (Table 1).

The estimated minimum trapping pressures for W-type FIs in Stage 3 range from 1 MPa to 68 MPa, corresponding to ore-forming depths under lithostatic to supra-lithostatic pressures. Hydrostatic pressures range from 0.01 km to 0.25 km and 0.01 km to 0.69 km, respectively (Table 1).

The maximum value of the mineralization pressure revealed by the minimum trapping pressure of W-type FIs in Stage 1, Stage 2, and Stage 3 of the Bailugou deposit is 183 MPa, 119 MPa, 68 MPa, which remains in decline accordingly from Stage 1 to Stage 2 and Stage 3. The pressures revealed by the C-type FIs in Stages 1 and 2 are 1157 MPa and 744 MPa, showing that the fluid pressure reduced from Stage 1 to Stage 2. The pressure revealed by the S-type FIs in Stage 1 is 76 MPa, showing that the captured pressure is relatively low, and the S-type FIs formed under the pressure reduction process.

The estimated maximum value of the formation depth of Stage 1, Stage 2, and Stage 3 revealed by the W-type FIs of the Bailugou deposit is 0.67 km, 0.44 km, 0.25 km under lithostatic pressure and 1.86 km, 1.22 km, 0.69 km under hydrostatic pressure. The depth revealed by C-type FIs from Stage 1 to Stage 2 is 4.22 km, 2.71 km under lithostatic pressure, 11.81 km, and 7.59 km under hydrostatic pressure, respectively. Summarily, the estimated formation depth of the Bailugou deposit was characterized as deep with a significant variation, which is about 2 km to 12 km and is much greater than the metallogenic limit of the epithermal hydrothermal gold deposit. Meanwhile, the ore formation depth varies greatly, a typical characteristic of fault-controlled deposits, as fluids can penetrate along faults at depths of up to 10 to 15 km [62,63]. The ductile-brittle transition appears as a structural, rheological, and thermal boundary separating an upper crust dominated by the percolation of meteoric, marine, and basin fluids and a lower crust marked by the circulation of magmatic and metamorphic fluids [64].

6.2. Temperature of Mineralization

6.2.1. Characteristic Temperature Revealed by Solid Solution Separation Structure

The chalcopyrite developed in sphalerite as a solid solution separation structure, or known as chalcopyrite disease [65], in the Bailugou deposit (Figure 6), reveals a corresponding formation temperature of 350° to 400 °C [66]. The eutectoid temperature point of solid solution minerals can be regarded as a geological thermometer; this temperature can be considered the lowest temperature for the separate mineralizing of sphalerite and chalcopyrite synchronously. Considering the guest mineral chalcopyrite is generally displayed as a beaded or emulsion droplet-like texture in the sphalerite as a solid solution separation structure while a few displayed as flakiness or leaf-like textures, indicating that, as the mineralizing of host mineral sphalerite, the temperature slowly decreased to the eutectoid point, micro-fine guest mineral chalcopyrite began to form in irregular orientation. After that, the temperature dropped sharply so that granular chalcopyrite could not gather and remain in the original separated location nearby, forming a random arrangement of emulsion droplets. With the continuous and slow temperature decline, a small amount of chalcopyrite gathered as linear, flakiness, and leaf-like droplets in cleavage in sphalerite with the directional arrangement. Meanwhile, the lack of board-like, knot-like, and polysynthetic guest mineral chalcopyrite in the solid solution separation structure confirms that the formation temperature is not too high. The formation of droplet structures may be related to the flow characteristics of the mineralizing fluid. The fluid movement within the ore body may have been relatively intense, causing mineral particles to precipitate in small, dispersed forms rather than aggregating into larger, flat lamellar or skeletal forms.

6.2.2. Homogenization Temperature of Fluid Inclusions

The homogenization temperature and peak value of fluid inclusions of Stage 1 to Stage 4 in the Bailugou deposit gradually decreased while the mineralization stages evolved. The overall mineralization temperature ranges between 400 °C and 100 °C (Table 1, Figure 11).

6.2.3. Equilibrium Temperature from Sulfur Isotope

The equilibrium temperatures calculated according to $\delta^{34}\text{S}$ values [67] by sulfide pairs such as pyrite–sphalerite, pyrite–galena, and sphalerite–galena of the Bailugou deposit are mainly clustered in the range of 351 °C to 585 °C, except two lower temperatures, 71 °C and 79 °C (Table 2). The $\Delta\delta^{34}\text{S}$ values of the two fractionations for the equilibrium temperatures of 71 °C and 79 °C are 3.0‰ and 5.9‰, respectively, which are relatively high. Excluding this temperature range for it may be the result of the destruction of the original equilibrium. Thereby, the reasonable sulfur isotope equilibrium temperature of the Bailugou deposit should be 351 °C to 585 °C, with $\Delta\delta^{34}\text{S}$ values of 1.3‰ to 1.9‰. This temperature is slightly higher than that of the S150 orebody calculated by Yan [45], which is 304 °C to 309 °C, and slightly higher than the homogenization temperature of FIs (100 °C to 400 °C). Still, it is

consistent with the common understanding that metal minerals' formation temperature is slightly higher than the homogenization temperature of FIs.

Table 2. Sulfur isotope geothermometer for Bailugou deposit.

Sample no.	Sampling Site	$\delta^{34}\text{S}_{\text{CDT}}/\text{‰}$			$\Delta\delta^{34}\text{S}/\text{‰}$	Temperature / $^{\circ}\text{C}$	Formula Source
		$\delta^{34}\text{S}_{\text{Py}}$	$\delta^{34}\text{S}_{\text{Sp}}$	$\delta^{34}\text{S}_{\text{Gn}}$			
BGL-14	S150, Gunligou	4.4	1.4		3.0	71	[68]
BGL-6	S150, Gunligou		9.1	7.2	1.9	351	
BLY-10	S170, Luyuangou		4.3	2.5	1.8	364	
BLY-19	S170, Luyuangou	3.9		2.5	1.4	585	[69]
BP-6	S116, Jiudinggou		3.4	2.1	1.3	476	
BQC-30	S170, Quancaigou		7.0	1.1	5.9	79	

Based on the above summarizations from the characteristic temperature revealed by the solid solution separation structure, the homogenization temperature of fluid inclusions, and the equilibrium temperature from sulfur isotope, this paper suggests that the temperature of mineral precipitation in the ore-forming fluid of Bailugou deposit is between 400 $^{\circ}\text{C}$ and 100 $^{\circ}\text{C}$, dominating concentrations from 400 $^{\circ}\text{C}$ to 350 $^{\circ}\text{C}$.

6.3. Origin, Evolution, and Precipitation Mechanism of Ore-Forming Fluids

Studies on the evolution of salinities, homogenization temperatures, and hydrogen-oxygen isotopes of fluid inclusions of different mineralization stages in the Bailugou deposit show that the initial ore-forming fluid was triggered under intense thermal-tectonic processes, associated with significant heat flow and tectonic movements, such as subduction, continental collision, or rifting. These processes dominated during the early and middle stages, which can lead to the generation of high-temperature fluids and create pathways for fluid migration. As it trended to the late stage, atmospheric precipitation gradually increased, and the contribution of surface waters to the mineralizing fluid grows significantly.

6.3.1. Fluid Immiscibility, Mixture, and Boiling

The evolution pattern of homogenization temperatures and salinities of the Bailugou deposit varies with the mineralization stages.

The fluid salinities in Stage 1 can be divided into two ends (Figure 12A). The lower salinities were mainly contributed by W-type and C-type FIs, with relatively higher homogenization temperatures (350 $^{\circ}\text{C}$ to 150 $^{\circ}\text{C}$) in the whole. In comparison, the higher salinities were primarily contributed by S-type FIs with lower homogenization temperatures (150 $^{\circ}\text{C}$). This pattern shows that the W-type, C-type, and S-type FIs in Stage 1 were not formed by fluid boiling but were more likely by fluid mixture followed by immiscibility. Considering the difference in homogenization temperatures, the W-type and C-type FIs should be formed from hydrothermal fluid, and the S-type FIs should be formed from the high-salinity fluid extracted from wall rocks. Although the Yanshanian (Jurassic–Cretaceous) granites have not been recognized in the Bailugou deposit, there are many intermediate-acid small intrusive bodies developed in this area (Figure 1). Bao et al. [70] speculated that there might exist a magma chamber deep in this area. Meanwhile, it was proved that, with the decrease in pressure and temperature, de-gassing, boiling, or immiscibility accompanied by the intruding of the granite can cause CO_2 release, and consequently, fluid condensation, pH increase, and oxygen fugacity decrease, followed by the massive precipitation of ore minerals [71–75], which should be the sufficient causes of the formation of the W-type and C-type FIs in the initial ore-forming fluid of the Bailugou deposit—the ore-bearing strata, the Longjiayuan, Sanchuan, Nannihu, Meiyaogou, Baishugou Fm. of the Luanchuan Group and the Guandaokou Group, regionally developed dolomite marble could be the potential extracting sources of high salinity

fluid. Meanwhile, the high enrichment of Pb, Zn, Ag, Mo, and W in ore-bearing strata showed by the geochemical characters [27,76,77] also verifies that the Luanchuan and Guandaokou Groups should be the favorite source for these metals.

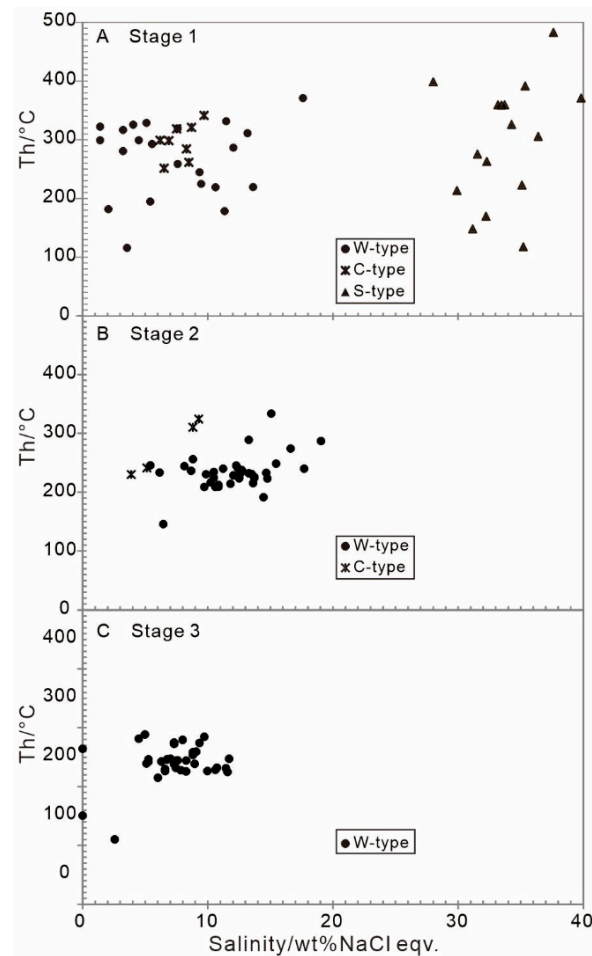


Figure 12. Homogenization temperatures versus salinities of fluid inclusions in different mineralization stages. (A) Stage 1; (B) Stage 2; (C) Stage 3.

The fluid salinities in Stage 2 tend to be more homogeneous, ranging from 5 wt.% to 18 wt.% NaCl equiv, which is comparable to the lower end of Stage 1's salinity (Figure 12B). The S-type FI assemblages with Th_{tot} values of daughter minerals over 550 °C observed in quartz in Stage 2 indicate the intensive fluid mixture of the hydrothermal fluid and the high-salinity fluid extracted from the ore-bearing strata.

The salinity of the fluid in Stage 3 was further decreased than in Stage 2. The observation of the C-type FI in Stage 3 indicates the fluid boiling, which was also confirmed by the observed petrography of FIs assemblages (Figure 9E,F) and the texture characteristics of ore minerals in this stage (Figure 6G). Still, the C-type FI is rare in number; therefore, no salinity of this type of FI in Stage 3 has been revealed (Figure 12C). The homogenization temperatures from Stage 2 to Stage 3 shown consist of non-significant decreases, which indicates the C-type FIs were released from fluid boiling caused by pressure reduction. The C-type FIs decrease with the evolution of the mineralization stages, which reveals gradual decreases in the pressure and shallower depth at the Bailugou deposit.

6.3.2. Genesis of the Bailugou Vein-Type Zinc-Lead-Silver Deposit

Combined with the geology, parameters from FIs, and the tectonic background of the study area, this paper first conducted the genetic types of the Bailugou deposit can be clas-

sified as orogenic metamorphic hydrothermal Pb–Zn–Ag deposit with the mineralization process as follows:

During Triassic to late Cretaceous, led by the subduction event in eastern China, the Late Mesozoic tectonic regime in this area was characterized by a transition from compression through transpressive compression (or transition from compression to extension) to extension, ending with continental collision during the late Cretaceous [15,67,78–80] (Figure 13A,B), along with intense tectonic-magmatic events [81–87]. The lithosphere in eastern China experienced a strong thinning process from the Late Jurassic to the Early Cretaceous [81,87,88], accompanied by these tectonic processes, large-scale granitic magmatic activity, such as small porphyry and large batholith, which were both developed in this intracontinental orogeny, known as the Yanshanian period [89]. The asthenospheric upwelling and underplating triggered deep penetration of the lower crust and the deeply sourced CO₂-rich ore-forming metamorphic hydrothermal solution was formed by the liquation process of deep rocks (strata and lower crust) under a high temperature, which is relatively slightly lower than the formation of magma caused by a gradient increase in temperature and pressure, triggered by the tectonic regime turned from collision to extension. The metamorphic hydrothermal solution mobilized and extracted ore-forming constituents from the siliceous banded strata, which were rich in metallogenic elements [27,76,77], dolomite marble and dolomite marble of the Luanchuan and Guandaokou Groups. Loading with the abundant metallogenic elements, the ore-forming fluid migrated upward along fault systems. It turned immiscible when it reached the brittle-ductile transition level (BDL, Figure 13C). This step leads to the ore-forming components rapidly precipitating as rough and euhedral crystals, due to fracturing and pressure drops. Meanwhile, it then rises to a shallow surface, joins with atmospheric precipitation due to the gradually developed open fracture system, and the low flow meteoric water along with the fractures and participate mixed with the deeply sourced hydrothermal, where fluid boiling might happen, resulting in the ore-forming constituents accumulated and deposited along with the fractures and interlayer detachment zones, formed the Bailugou Pb–Zn–Ag deposit (Figure 13). The research of H–O–C–S–Pb isotope geochemistry from Yang et al. [67] also support this view.

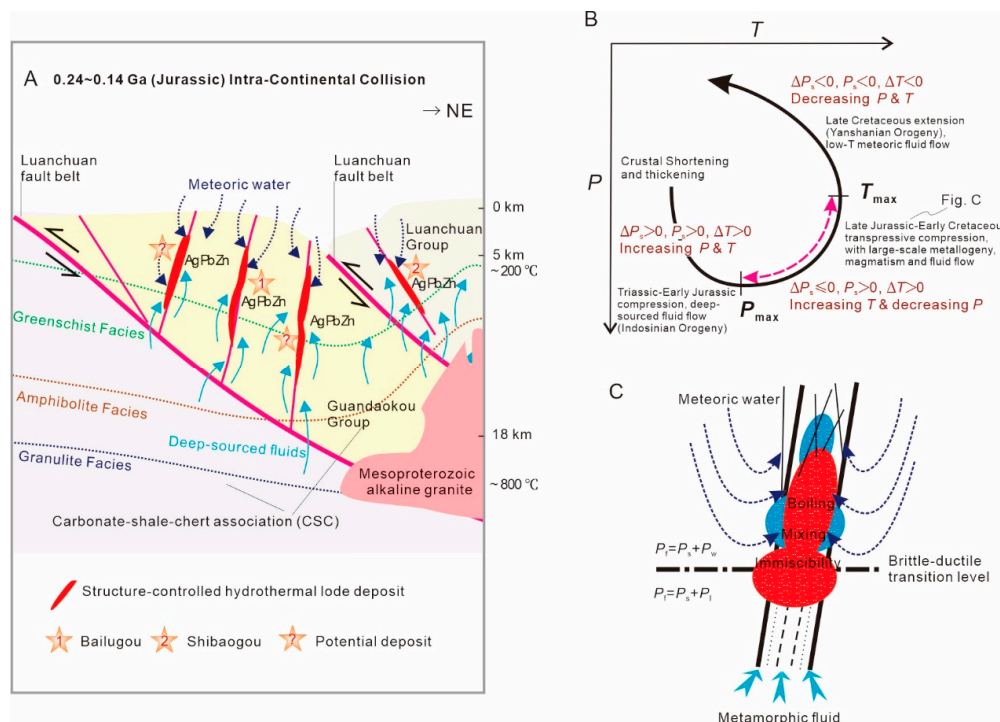


Figure 13. Tectonic evolution and genetic model for the Bailugou deposit. (A) Schematic representation of CMF (collisional orogeny, metallogeny and fluid flow) showing the relationships between ore-hosting

structures, granitoids, porphyries and deposits in Bailugou area. Fluids, released from subducted slab and sediment or from the hydrated mantle wedge at granulite facies, travel up-dip along the interface between the slab and the overlying wedge or base of the lithosphere at amphibolite facies. The over-pressured ore fluids intersect deep crustal faults and then advent upwards to form orogenic deposits in second-order structures or hydraulically fractured rock bodies at greenschist facies. (B) P – T – t path for collisional orogeny showing a three-stage geodynamic process and the P – T conditions for fluid generation, petrogenesis and metallogenesis from Triassic to Cretaceous in Luanchuan area, East Qinling Orogeny. (C) Cartoons illustrating the formation process of Bailugou ore deposit. Abbreviations: P_f , fluid pressure; P_s , structural overpressure; P_l , lithostatic pressure; P_w , hydrostatic pressure; ΔT , variation in temperature; ΔP_s , variation in structural overpressure.

7. Conclusions

(1) The Bailugou lead-zinc-silver deposit is situated within the siliceous banded dolomite marble and dolomite marble of the Luanchuan and Guandaokou Groups of the Middle-Late Proterozoic. This deposit is firstly categorized as an orogenic metamorphic epi-mesothermal deposit, arising from complex, multi-stage hydrothermal processes.

(2) During an intense tectonic-thermal process, the initial ore-forming fluid is triggered. This fluid underwent a transformation from a metamorphic hydrothermal solution to a meteoric hydrothermal solution as it progresses through the mineralization stages. Throughout this process, it experiences fluid immiscibility, mixing, and boiling with metamorphic water.

(3) The genesis of the ore-forming constituents appears to be multi-sourced, as inferred from analyses of fluid inclusions. The ore-forming materials of Bailugou deposit derives mainly from a combination of the ore-bearing strata Meiyaogou Formation and Nannihu Formation within the Luanchuan and Guandaokou Groups.

Author Contributions: Conceptualization, Y.Y. and Y.C.; methodology, Y.Y.; formal analysis and investigation, Y.Y., N.G. and D.W.; writing—original draft preparation, N.G. and D.W.; writing—review and editing, Y.Y., H.C. and Y.C.; supervision, Z.P.; project administration, H.C.; funding acquisition, Y.C. All authors have read and agreed to the published version of the manuscript.

Funding: This research was funded by the National Nature Science Foundation of China, grant number 41702098, 42202073 and 40702013, the National Key Research and Development Program of China, grant number 2021YFC2900300, the China Geological Survey Project, grant number DD20230355, DD20230356 and DD20242591 and the Key Program of the National Natural Science Foundation of China, grant number U2244206 and 41630313.

Data Availability Statement: The data presented in this study are available on request from the corresponding author. The data are not publicly available due to Privacy.

Acknowledgments: The authors extend gratitude to Jinping Qi, Jing Li, Jiangwei Han and the Henan Bureau of Geological Exploration for Non-ferrous Metals for supporting this field investigation. We also thank the academic editor Giorgio Garuti, managing editor Kimura Xia, assistant editor Cassie Zhou and anonymous reviewers for their valuable suggestions and feedback.

Conflicts of Interest: The authors declare no conflicts of interest regarding the publication of this article.

References

1. Beck, R.; Weed, W.H. *The Nature of Ore Deposits*; McGraw-Hill: New York, NY, USA, 1909; p. 685.
2. Lindgren, W. *Mineral Deposits*; McGraw-Hill: New York, NY, USA, 1933; p. 930.
3. Hammer, D.F.; Peterson, D.W. Geology of the Magma Mine Area, Arizona. In *Ore Deposits of the United States*; Ridge, J.D., Ed.; The American Institute of Mining, Metallurgical, and Petroleum Engineers, Inc.: New York, NY, USA, 1968; Volume 1933–1967, pp. 1282–1310.
4. Rye, R.O.; Sawkins, F. Fluid inclusion and stable isotope studies on the Casapalca Ag-Pb-Zn-Cu deposit, Central Andes, Peru. *Econ. Geol.* **1974**, *87*, 225–262. [[CrossRef](#)]
5. Guilbert, J.M.; Park, C.F. *The Geology of Ore Deposits*; Freeman: San Francisco, CA, USA, 1986; p. 985.

6. Graybeal, F.T.; Smith, D.M., Jr.; Vikre, P.G. The geology of silver deposits. In *Handbook of Strata-Bound and Stratiform Ore Deposits*; Wolf, K.H., Ed.; Springer: Berlin/Heidelberg, Germany, 1986; Volume 14, pp. 1–184.
7. Keith, J.D.; Whitney, J.A.; Hattori, K.; Ballantyne, G.H.; Christiansen, E.H.; Barr, D.L.; Cannan, T.M.; Hook, C.J. The role of magmatic sulfides mafic alkaline magmas in the Bingham Tintic Mining Districts Utah. *J. Petrol.* **1997**, *38*, 1679–1690. [[CrossRef](#)]
8. Kissin, S.A.; Mango, H. Silver vein deposits. In *Treatise on Geochemistry*, 2nd ed.; Elsevier: Oxford, UK, 2014; pp. 425–432.
9. Im, H.; Jeong, J.; Shin, D. Genetic environment of W skarn and Pb-Zn vein mineralization associated with the Imog granite in the Taebaeksan Mineralized District, South Korea. *Ore Geol. Rev.* **2020**, *126*, 103721. [[CrossRef](#)]
10. Beaudoin, G.; Sangster, D.F. A descriptive model for silver-lead-zinc veins in clastic metasedimentary terranes. *Econ. Geol.* **1992**, *87*, 1005–1021. [[CrossRef](#)]
11. Lynch, J.V.G.; Longstaffe, F.J.; Nesbitt, B.E. Stable isotopic and fluid inclusion indications of large-scale hydrothermal paleo flow, boiling, and fluid mixing in the Keno Hill Ag-Pb-Zn district, Yukon Territory, Canada. *Geochim. Cosmochim. Acta* **1990**, *54*, 1045–1059. [[CrossRef](#)]
12. Leach, D.L.; Landis, G.P.; Hofstra, A.H. Metamorphic origin of the Coeur d’Alene base-and precious-metal veins in the Belt basin, Idaho and Montana. *Geology* **1988**, *16*, 122–125. [[CrossRef](#)]
13. Leach, D.L.; Hofstra, A.H.; Church, S.E.; Snee, L.W.; Vaughn, R.B.; Zartman, R.E. Evidence for Proterozoic and Late Cretaceous–Early Tertiary ore-forming events in the Coeur d’Alene district, Idaho and Montana. *Econ. Geol.* **1998**, *93*, 347–359. [[CrossRef](#)]
14. Johnson, C.A.; Cardellach, E.; Tritlla, J.; Hanan, B.B. Cierco Pb-Zn-Ag vein deposits: Isotopic and fluid inclusion evidence for formation during the Mesozoic extension in the Pyrenees of Spain. *Econ. Geol.* **1996**, *91*, 497–506. [[CrossRef](#)]
15. Chen, Y.J.; Pirajno, F.; Sui, Y.H. Isotope geochemistry of the Tieluping silver deposit, Henan, China: A case study of orogenic silver deposits and related tectonic setting. *Miner. Depos.* **2004**, *39*, 560–575. [[CrossRef](#)]
16. Qi, J.P.; Chen, Y.J.; Ni, P.; Lai, Y.; Ding, J.Y.; Song, Y.W.; Tang, G.J. Fluid inclusion constraints on the origin of the Lengshuibeiyou Pb-Zn-Ag deposit, Henan province. *Acta Petrol. Sin.* **2007**, *23*, 2119–2130. (In Chinese with English Abstract)
17. Zhang, J.; Yang, Y.; Hu, H.Z.; Wang, Z.G.; Li, G.P.; Li, Z.L. C-S-Pb isotope geochemistry of the Yindonggou orogenic type silver deposit in Henan Province. *Acta Petrol. Sin.* **2009**, *25*, 2833–2842. (In Chinese with English Abstract)
18. Zhang, J.; Yang, Y.; Lu, Y.H. Lead isotope geochemistry of the Weishancheng gold-silver ore belt, Henan Province, China: Implications for ore genesis. *Acta Petrol. Sin.* **2009**, *25*, 444–454. (In Chinese with English Abstract)
19. Zhang, J.; Chen, Y.J.; Yang, Y.; Deng, J. Lead isotope systematics of the Weishancheng Au–Ag belt, Tongbai Mountains, central China: Implication for ore genesis. *Int. Geol. Rev.* **2011**, *53*, 656–676. [[CrossRef](#)]
20. Li, Z.K.; Li, J.W.; Zhao, X.F.; Zhou, M.F.; Selby, D.; Bi, S.J.; Sui, J.X.; Zhao, Z.J. Crustal-extension Ag-Pb-Zn veins in the Xiong’ershan district, southern North China Craton: Constraints from the Shagou Deposit. *Econ. Geol.* **2013**, *108*, 1703–1729. [[CrossRef](#)]
21. Han, J.S.; Yao, J.M.; Chen, H.Y.; Deng, X.H.; Ding, J.Y. Fluid inclusion and stable isotope study of the Shagou Ag-Pb-Zn deposit, Luoning, Henan province, China: Implications for the genesis of an orogenic lode Ag-Pb-Zn system. *Ore Geol. Rev.* **2014**, *62*, 199–210. [[CrossRef](#)]
22. Zhang, J.; Chen, Y.J.; Su, Q.W.; Zhang, X.; Xiang, S.H.; Wang, Q.S. Geology and genesis of the Xiaguan Ag–Pb–Zn orefield in Qinling orogen, Henan province, China: Fluid. inclusion and isotope constraints. *Ore Geol. Rev.* **2016**, *76*, 79–93. [[CrossRef](#)]
23. Chen, X.L.; Shao, Y.J.; Lai, C.; Wang, C. Genesis of the Longmendian Ag–Pb–Zn Deposit in Henan (Central China): Constraints from Fluid Inclusions and H–C–O–S–Pb Isotopes. *Geofluids* **2020**. [[CrossRef](#)]
24. Yang, Y.; Chen, Y.J.; Zhang, J.; Zhang, C. Ore geology, fluid inclusions and four-stage hydrothermal mineralization of the Shangfanggou giant Mo–Fe deposit in Eastern Qinling, central China. *Ore Geol. Rev.* **2013**, *55*, 146–161. [[CrossRef](#)]
25. Yang, Y.; Liu, Z.J.; Deng, X.H. Mineralization mechanisms in the Shangfanggou giant porphyry-skarn Mo-Fe deposit of the east Qinling, China: Constraints from H–O–C–S–Pb isotopes. *Ore Geol. Rev.* **2017**, *81 Pt 2*, 535–547. [[CrossRef](#)]
26. Qi, J.P.; Song, Y.W.; Li, S.Q.; Chen, F.K. Single-grain Rb-Sr isotopic composition of the Xigou Pb-Zn-Ag deposit, Luanchuan, Henan province. *Acta Petrol. Sin.* **2009**, *25*, 2843–2854, (In Chinese with English Abstract).
27. Qi, J.P. Geology, Geochemistry and Genesis of Vein-Type Zn-Pb-Silver Deposits in Luanchuan, Henan. Ph.D. Thesis, Peking University, Beijing, China, 2006; pp. 1–133, (In Chinese with English Abstract).
28. Fyfe, W.S.; Price, N.J.; Thompson, A.B. *Fluids in the Earth’s Crust*; Elsevier: Amsterdam, The Netherlands, 1978; p. 383.
29. Etheridge, M.A.; Wall, V.J. The role of the fluid phase during regional metamorphism and deformation. *J. Metamorph. Geol.* **1983**, *1*, 205–226. [[CrossRef](#)]
30. Thompson, A.B.; Connolly, J.A.D. Migration of metamorphic fluid: Some aspects of mass and heat transfer. *Earth-Sci. Rev.* **1992**, *32*, 107–121. [[CrossRef](#)]
31. Taylor, H.P., Jr. The application of oxygen and hydrogen isotope studies to problems of hydrothermal alteration and ore deposition. *Econ. Geol.* **1974**, *69*, 843–883. [[CrossRef](#)]
32. Taylor, H.P., Jr. Oxygen and hydrogen isotope relationships in hydrothermal mineral deposits. In *Geochemistry of Hydrothermal Ore Deposits*, 3rd ed.; Barnes, H.L., Ed.; Wiley: New York, NY, USA, 1997; pp. 229–302.
33. Arndt, N.; Ganino, C. Hydrothermal deposits. In *Metals and Society, An Introduction to Economic Geology*; Springer: Berlin/Heidelberg, Germany, 2012; pp. 73–112.
34. Steven, M.; Heather, A.S.; Timothy, B. Active fault and shear processes and their implications for mineral deposit formation and discovery. *J. Struct. Geol.* **2010**, *32*, 151–165. [[CrossRef](#)]

35. Duan, S.G.; Xue, C.J.; Liu, G.Y.; Yan, C.H.; Feng, Q.W.; Song, Y.W.; Gao, B.Y. Geology, fluid inclusions and stable isotopic geochemistry of Bailugou Pb–Zn deposit in Luanchuan area, Henan Province. *Miner. Depos.* **2010**, *29*, 810–825. (In Chinese with English Abstract)
36. Duan, S.G.; Xue, C.J.; Liu, G.Y.; Yan, C.H.; Feng, Q.W.; Song, Y.W.; Tu, Q.J.; Gao, Y.; Gao, B.Y. Ceology and sulfur isotope geochemistry of lead-zinc deposits in Luanchuan district, Henan Province, China. *Earth Sci. Front.* **2010**, *17*, 375–384. (In Chinese with English Abstract)
37. Duan, S.G.; Xue, C.J.; Feng, Q.W.; Gao, B.Y.; Liu, G.Y.; Yan, C.H.; Song, Y.W. Geology, fluid inclusions and S, Pb isotopic geochemistry of the Chitudian Pb–Zn deposit in Luanchuan, Henan Province. *Geol. China* **2011**, *38*, 427–441. (In Chinese with English Abstract)
38. Duan, S.G.; Xue, C.J.; Chi, G.X.; Liu, G.Y.; Yan, C.H.; Feng, Q.W. Ore geology, fluid inclusion, and S- and Pb-isotopic constraints on the genesis of the Chitudian Zn–Pb deposit, southern margin of the North China Craton. *Resour. Geol.* **2011**, *61*, 224–240. [[CrossRef](#)]
39. Cao, H.W.; Zhang, S.T.; Santosh, M.; Zheng, L.; Tang, L.; Li, D.; Zhang, X.H.; Zhang, Y.H. The Luanchuan Mo–W–Pb–Zn–Ag magmatic–hydrothermal system in the East Qinling metallogenic belt, China: Constrains on metallogenesis from C–H–O–S–Pb isotope compositions and Rb–Sr isochron ages. *J. Asian Earth Sci.* **2015**, *111*, 751–780. [[CrossRef](#)]
40. Zhang, H.Q. Geochemical characteristics and geological significance of the Bailugou Pb–Zn–Ag deposit in Henan Province. *Miner. Explor.* **2021**, *12*, 2069–2075. (In Chinese with English Abstract)
41. Xu, Y.; Wang, G.; Gao, M.; Yang, W.; Yang, S.; Yun, H.; Wu, P.; Guo, N.; Feng, Y. Genesis of the Shibaogou Mo–Pb–Zn deposit in the Luanchuan ore district, China: Constraints from geochronology, fluid inclusion, and H–O–S–Pb isotopes. *Front. Earth Sci.* **2023**, *10*, 1032183. [[CrossRef](#)]
42. Li, N.; Chen, Y.J.; Zhang, H.; Zhao, T.P.; Deng, X.H.; Wang, Y.; Ni, Z.Y. Molybdenum deposits in East Qinling. *Earth Sci. Front.* **2007**, *14*, 186–198. (In Chinese with English Abstract)
43. Hu, S.X.; Lin, Q.L.; Chen, Z.M.; Li, S.M. *Geology and Metallogeny of the Collision Belt Between North China Plates*; Nanjing University Press: Nanjing, China, 1988; p. 558. (In Chinese)
44. Lü, W.D.; Sun, W.Z. Metallogenic condition of lead and zinc deposit in Lushi–Lanchuan terrain. *Miner. Resour. Geol.* **2004**, *18*, 507–516. (In Chinese with English Abstract)
45. Yan, C.H. *Study on Inner Structure of Lead-Zinc-Silver Mineralization System in Eastern Qinling*; Geological Publishing House: Beijing, China, 2004; p. 144. (In Chinese with English Abstract)
46. Lu, S.N.; Li, H.K.; Li, H.M.; Song, B.; Wang, S.Y.; Zhou, H.Y.; Chen, Z.H. U–Pb isotopic ages and their significance of Alkaline Granite in the southern margin of the North China Craton. *Geol. Bull. China* **2003**, *22*, 762–768. (In Chinese with English Abstract)
47. Yan, C.H.; Liu, G.Y.; Peng, Y.; Song, Y.W.; Wang, J.Z.; Zhao, R.J.; Zeng, X.Y.; Lü, W.D.; Yao, X.N.; Ma, H.W.; et al. *The Metallogenic Regularity of Lead-Zinc Ore in the Southwest Hernan Province*; Geological Publishing House: Beijing, China, 2009; p. 369. (In Chinese with English Abstract)
48. Roedder, E. Fluid inclusions. Reviews in mineralogy. *Miner. Soc. Am.* **1984**, *12*, 644.
49. Diamond, L.W. Review of the systematics of CO₂–H₂O fluid inclusions. *Lithos* **2001**, *55*, 69–99. [[CrossRef](#)]
50. Burke, E.A.J. Raman microspectrometry of fluid inclusions. *Lithos* **2001**, *55*, 139–158. [[CrossRef](#)]
51. Bozzo, A.T.; Chen, H.S.; Kass, J.R.; Barduhn, A.J. The properties of hydrates of chlorine and carbon dioxide. *Desalination* **1975**, *16*, 303–320. [[CrossRef](#)]
52. Potter, R.W.; Clynnne, M.A.; Brown, D.L. Freezing point depression of aqueous Sodium Chloride Solutions. *Econ. Geol.* **1978**, *73*, 284–285. [[CrossRef](#)]
53. Hall, D.L.; Sterner, S.M.; Bodner, R.J. Freezing point depression of NaCl–KCl–H₂O solutions. *Econ. Geol.* **1988**, *83*, 197–202. [[CrossRef](#)]
54. Bodnar, R.J. Reviced equation and table for determining the freezing point depression of H₂O–NaCl solutions. *Geochim. Cosmochim. Acta* **1993**, *57*, 683–684. [[CrossRef](#)]
55. Sterner, S.M.; Hall, D.L.; Bodnar, R.J. Synthetic fluid inclusions—V. Solubility relations in the system NaCl–KCl–H₂O under vapor-saturated conditions. *Geochim. Cosmochim. Acta* **1988**, *52*, 989–1005. [[CrossRef](#)]
56. Brown, P.E. FLINCOR: A microcomputer program for the reduction and investigation of fluid-inclusion data. *Am. Mineral.* **1989**, *74*, 1390–1393.
57. Brown, P.E.; Lamb, W.M. P–V–T properties of fluids in the system H₂O–CO₂–NaCl: New graphical presentations and implications for fluid inclusion studies. *Geochim. Cosmochim. Acta* **1989**, *53*, 1209–1221. [[CrossRef](#)]
58. Haas, J.L. Physical properties of the coexisting phases and thermochemical properties of the H₂O component in boiling NaCl solutions. *US Geol. Surv. Bull.* **1976**, *1421A*, 73.
59. Bodnar, R.J. A method of calculating fluid inclusion volumes based on vapor bubble diameters and PVTX properties of inclusion fluids. *Econ. Geol.* **1983**, *78*, 535–542. [[CrossRef](#)]
60. Bischoff, J.L. Densities of liquids and vapors in boiling NaCl–H₂O solutions: A PVTX summary from 300 °C to 500 °C. *Amer. J. Sci.* **1991**, *291*, 309–338. [[CrossRef](#)]
61. Bowers, T.S.; Helgeson, H.C. Calculation of the thermodynamic and geochemical consequences of nonideal mixing in the system H₂O–CO₂–NaCl on phase relations in geologic systems: Equation of state for H₂O–CO₂–NaCl fluids at high pressures and temperatures. *Geochim. Cosmochim. Acta* **1983**, *47*, 1247–1275. [[CrossRef](#)]

62. Wickham, S.M.; Peters, M.T.; Fricke, H.C.; O'Neil, J.R. Identification of magmatic and meteoric fluid sources and upward- and downward-moving infiltration fronts in a metamorphic core complex. *Geology* **1993**, *21*, 81–84. [[CrossRef](#)]
63. Famin, V.; Philippot, P.; Jolivet, L.; Agard, P. *Evolution of Hydrothermal Regime along a Crustal Shear Zone*; Tectonics: Tinos Island, Greece, 2004; Volume 23, pp. 1–23.
64. Siebenaller, L.; Boiron, M.C.; Vanderhaeghe, O.; Hibsich, C.; Jessell, M.W.; André-Mayer, A.S.; France-Lanord, C.; Photiades, A. Fluid record of rock exhumation across the brittle ductile transition during formation of a metamorphic core complex (Naxos Island, Cyclades, Greece). *J. Metamorph. Geol.* **2013**, *31*, 313–338. [[CrossRef](#)]
65. Paul, B.B.; Philip, M.B. Chalcopyrite disease in sphalerite; pathology and epidemiology. *Am. Mineral.* **1987**, *72*, 451–467.
66. Shang, J.; Lu, J.W.; Peng, X.L.; Zhang, Y. *Mineragraphy*; Geological Publishing House: Beijing, China, 2007; p. 156. (In Chinese with English Abstract)
67. Yang, Y.; Chen, H.; Guo, N.N.; Wu, D.H.; Pang, Z.S.; Chen, Y.J. Isotope Geochemistry and Metallogenic Model of the Bailugou Vein-Type Zn-Pb-Ag Deposit, Eastern Qinling Orogen, China. *Minerals*, 2024; *submitted*.
68. Sakai, H. Isotopic properties of sulfur compounds in hydrothermal processes. *Geochem. J.* **1968**, *2*, 29–49. [[CrossRef](#)]
69. Ohmoto, H.; Rye, R.O. Isotopes of Sulfur and Carbon. In *Geochemistry of Hydrothermal Ore Deposits*; Barnes, H.L., Ed.; Wiley-Interscience: New York, NY, USA, 1979; pp. 509–567.
70. Bao, Z.W.; Zeng, Q.S.; Zhao, T.P.; Yuan, Z.L. Geochemistry and petrogenesis of the ore related Nannihu and Shangfanggou granite porphyries from east Qinling belt of molybdenum mineralization. *Acta Petrol. Sin.* **2009**, *25*, 2523–2536. (In Chinese with English Abstract)
71. Fogel, R.A.; Rutherford, M.J. The solubility of carbon dioxide in rhyolitic melts: A quantitative FTIR study. *Am. Mineral.* **1990**, *75*, 1311–1326.
72. Giggenbach, W.F. The origin and evolution of fluids in magmatic-hydrothermal systems. In *Geochemistry of Hydrothermal Ore Deposits*; Barnes, H.L., Ed.; Kidston Gold Mines Company Report; Kidston Gold Mines Company: Einasleigh, QLD, Australia, 1997; p. 82.
73. Lowenstern, J. B A review of the contrasting behavior of two magmatic volatiles: Chlorine and carbon dioxide. *J. Geochem. Explor.* **2000**, *69–70*, 287–290. [[CrossRef](#)]
74. Lowenstern, J.B. Carbon dioxide in magmas and implications for hydrothermal systems. *Miner. Depos.* **2001**, *36*, 490–502. [[CrossRef](#)]
75. Chen, Y.J.; Ni, P.; Fan, H.R.; Pirajno, F.; Lai, Y.; Su, W.C.; Zhang, H. Diagnostic fluid inclusions of different types hydrothermal gold deposits. *Acta Petrol. Sin.* **2007**, *23*, 2085–2108. (In Chinese with English Abstract)
76. Li, Y.F. The Temporal-Spatial Evolution of Mesozoic Granitoids in the Xiong'ershan Area and Their Relationships to Molybdenum-Gold Mineralization. Ph. D. Dissertation, University of Geosciences, Beijing, China, 2005; pp. 1–135. (In Chinese with English Summary)
77. Ye, H.S. The Mesozoic tectonic evolution and Pb-Zn-Ag metallogeny in the southern margin of North China Craton. Ph.D. Dissertation, Chinese Academy of Geological Sciences, Beijing, China, 2006; pp. 1–225. (In Chinese with English Summary)
78. Chen, Y.J.; Sui, Y.H.; Pirajno, F. Exclusive evidences for CMF model and a case of orogenic silver deposits: Isotope geochemistry of the Tieluping silver deposit, east Qinling orogen. *Acta Petrol. Sin.* **2003**, *19*, 551–568. (In Chinese with English Abstract)
79. Chen, Y.J.; Pirajno, F.; Sui, Y.H. Geology and D–O–C isotope systematics of the Tieluping silver deposit, Henan, China: Implications for ore genesis. *Acta Geol. Sin.* **2005**, *79*, 106–119. (In Chinese with English Abstract)
80. Chen, Y.J.; Pirajno, F.; Qi, J.P.; Li, J.; Wang, H.H. Ore geology, fluid geochemistry and genesis of the Shanggong gold deposit, eastern Qinling Orogen, China. *Resour. Geol.* **2006**, *56*, 99–116. [[CrossRef](#)]
81. Yang, F.; Santosh, M.; Kim, S.W. Mesozoic magmatism in the eastern North China Craton: Insights on tectonic cycles associated with progressive craton destruction. *Gondwana Res.* **2018**, *60*, 153–178. [[CrossRef](#)]
82. Li, N.; Chen, Y.-J.; Santosh, M.; Pirajno, F. Late Mesozoic granitoids in the Qinling Orogen, central China, and tectonic significance. *Earth. Sci. Rev.* **2018**, *182*, 141–173. [[CrossRef](#)]
83. Xue, F.; Wang, G.W.; Santosh, M.; Yang, F.; Shen, Z.W.; Kong, L.; Guo, N.; Zhang, X.; Jia, W. Geochemistry and geochronology of ore-bearing and barren intrusions in the Luanchuan ore fields of East Qinling metallogenic belt, China: Diverse tectonic evolution and implications for mineral exploration. *J. Asian Earth Sci.* **2018**, *157*, 57–77. [[CrossRef](#)]
84. Xue, F.; Santosh, M.; Tsunogae, T.; Yang, F. Geochemical and isotopic imprints of early cretaceous mafic and felsic dyke suites track lithosphere- asthenosphere interaction and craton destruction in the North China Craton. *Lithos* **2019**, *326–327*, 174–199. [[CrossRef](#)]
85. Xue, F.; Santosh, M.; Tsunogae, T.; Yang, F.; Zhou, H. The Genesis of high Ba-Sr adakitic rocks: Insights from an Early Cretaceous volcanic suite in the central North China Craton. *Geol. J.* **2020**, *55*, 5398–5416. [[CrossRef](#)]
86. Tang, L.; Hu, X.K.; Santosh, M.; Zhang, S.T.; Spencer, C.J.; Jeon, H.; Zhao, Y.; Cao, H.-W. Multistage processes linked to tectonic transition in the Genesis of orogenic gold deposit: A case study from the Shanggong lode deposit, East Qinling, China. *Ore Geol. Rev.* **2019**, *111*, 102998. [[CrossRef](#)]
87. Yang, F.; Xue, F.; Santosh, M.; Wang, G.; Kim, S.W.; Shen, Z.; Jia, W.; Zhang, X. Late Mesozoic magmatism in the East Qinling Orogen, China and its tectonic implications. *Geosci. Front.* **2019**, *10*, 1803–1821. [[CrossRef](#)]

88. Yang, F.; Santosh, M.; Tang, L. Extensive crustal melting during craton destruction: Evidence from the Mesozoic magmatic suite of Junan, eastern North China Craton. *J. Asian Earth Sci.* **2018**, *157*, 119–140. [[CrossRef](#)]
89. Zhang, G.W.; Meng, Q.R.; Yu, Z.P.; Li, J.; Wang, Y.; Liu, H.; Chen, X.; Zhao, M.; Wu, T.; Xu, L.; et al. Orogenesis and dynamics of Qinling orogen. *Sci. China* **1996**, *26*, 193–200. (In Chinese)

Disclaimer/Publisher’s Note: The statements, opinions and data contained in all publications are solely those of the individual author(s) and contributor(s) and not of MDPI and/or the editor(s). MDPI and/or the editor(s) disclaim responsibility for any injury to people or property resulting from any ideas, methods, instructions or products referred to in the content.